

# 國立交通大學

光電工程學系

碩士論文

兆赫波段可調式液態晶體 Solc 濾波器

**A Liquid-Crystal-Based Terahertz Tunable Solc Filter**



研究生：何宜貞

指導教授：潘犀靈 教授

中華民國九十六年七月

兆赫波段可調式液態晶體 Solc 濾波器  
**A Liquid-Crystal-Based Terahertz Tunable Solc Filter**

研究生：何宜貞

Student : I-Chen Ho

指導教授：潘犀靈

Advisor : Ci-Ling Pan

國立交通大學

光電工程學系

碩士論文

A Thesis

Submitted to Institute of Electro-Optical Engineering & Department of Photonics

College of Electrical and Computer Engineering

National Chiao Tung University

in partial Fulfillment of the Requirements

for the Degree of

Master

in

Photonics

July 2007

Hsinchu, Taiwan, Republic of China

中華民國九十六年七月

# 兆赫波段可調式液態晶體 Solc 濾波器

學生：何宜貞

指導教授：潘犀靈

國立交通大學光電工程學系（研究所）碩士班

## 摘 要

我們研製了一種兆赫波段可調式 Solc 濾波器，實驗數據與理論預測相符合。利用外加磁場控制向列型液晶(E7)的雙折射性，可在室溫下連續調變穿透頻率從 0.176 至 0.793 THz (中心頻率之調幅可達 350%)；此濾波器之置入能量損耗為 5dB。為了改善置入能量損失、使用便利性與快速反應等因素，我們也設計了一種電場控制向列型液晶(E7)之 Solc 濾波器，在室溫下連續可調範圍從 0.717 到 1.142 THz (中心頻率之調幅可達 59%)。我們也量測具較大雙折射性( $\Delta n \sim 0.18$ )向列型液晶 (DN125262W) 的折射係數並利用此材料製作 Solc 濾波器，與 E7 相同濾波效果下，此濾波器操作在較低頻區( $< 0.7$  THz)，置入性損耗減少  $\sim 1.5$  dB。

# A Liquid-Crystal-Based Terahertz Tunable Solc Filter

student : I-Chen Ho

Advisors : Dr. Ci-Ling Pan

Department (Institute) of Photonics  
National Chiao Tung University

## ABSTRACT

A large tunable range, room-temperature terahertz Solc filter has been demonstrated. The first central pass-band frequency of the device can be continuously tuned from 0.176 to 0.793 THz (a fractional tuning range of 350%) using magnetically controlled birefringence in the nematic liquid crystals (E7). The insertion loss of the present device is about 5 dB. We also designed and constructed an electrically controlled, tunable terahertz Solc filter of which the central pass-band frequency can be continuously tuned from 0.717 to 1.142 THz (a fractional tuning range of 59%). The electrically tuned filter has advantages of compact use, ease in control, fast response, and low insertion loss. Moreover, we have investigated a commercial liquid crystal DN125262W with large birefringence and applied it for filtering applications. It can operate at low frequencies ( $< 0.7$  THz).and the insertion loss reduce  $\sim 1.5$ dB, comparing with E7. The results are in good agreement with theoretic predictions.

## 誌 謝

何其榮幸能在交大度過兩年的碩士生學習，對這裡的一切充滿著極大的不捨，潘犀靈教授亦師亦父的教導和趙如蘋教授無私的提供實驗與技術上的指導，使我能更深的進入科學的核心。然而實驗室的博士班學長們，以及同學與學弟妹，更是讓我在每天的生活中充滿驚奇與樂趣，尤其難忘的是碩一修課時，和同學們討論作業與合作找資料的成就感。



更感謝父母在我求學生涯的支持與關心，雖然是耳提面命也是我最甜蜜的支柱。當然還有紹文姊姊，謝謝妳讓我每天拖著疲憊的身體回家時，可以完全的放鬆自己。最後謝謝正凱，你總是在我最需要幫助的時候，犧牲自己的時間使我能做到最好，希望你也能達成你的夢想。

宜貞 2007/7/24

# Contents

<b>Abstract (Chinese)</b>	<b>I</b>
<b>Abstract (English)</b>	<b>II</b>
<b>Acknowledgements</b>	<b>III</b>
<b>Contents</b>	<b>IV</b>
<b>Tables</b>	<b>VI</b>
<b>List of Figures</b>	<b>VII</b>
<b>Chapter 1. Introduction</b>	<b>1</b>
1.1. Terahertz technology: Terahertz Filter	2
1.2. Nematic Liquid Crystal	3
1.3. Thesis highlights	6
1.4. References	8
<b>Chapter 2. Terahertz Time-domain-spectroscopy (THz-TDS)</b>	<b>10</b>
2.1. Introduction	10
2.2. Schematic setup of THz-TDS radiation using PC antenna	10
2.3. Generation of THz radiation Using PC antenna	14
2.4. Detection of THz-TDS radiation using PC antenna	16
2.5. The application of THz-TDS: extracting the refractive index of a large birefringence LC-DN125262W	19
2.6. References	26

### **Chapter 3. Magnetically Controlled Liquid-Crystal-Based Terahertz**

<b>Tunable Solc Filter</b>	<b>27</b>
3.1. Introduction	27
3.2. Theory of Solc filter	28
3.3. Design and measurement	30
3.4. Results	35
3.5. Discussion	39
3.6. Comparison with our previous work: a THz Lyot filter	41
3.7. Summary	42
3.8. References	43

### **Chapter 4. Electrically Controlled Liquid-Crystal-Based Terahertz**

<b>Tunable Solc Filter</b>	<b>45</b>
4.1. Introduction	45
4.2. Previous evaluation	45
4.3. Sample preparation and setup	46
4.4. Results and discussion	50
4.5. A four-stage folded cascaded Solc filter	53
4.6. Improvement	55
4.7. Summary	56
4.8. References	57

### **Chapter 5. Conclusion and Future Work**

**58**

# Tables

**Table 2.1.** The measuring results of refractive indices between different thicknesses of DN125262W cells, and one thickness E7 cell. **25**

**Table 3.1.** The comparison of Lyot and Solc filter in THz range. **41**





# List of Figures

<b>Fig. 1.1.</b> The diagram defines the name of electromagnetic wave in different frequency ranges.	1
<b>Fig. 1.2. (a)</b> The experimental diagram of the LC-based tunable THz Lyot filter. (b) The peak transmitted frequencies of the filter vs different time delay, $\Delta\tau_A$ . The circles are experimental data and the curve is theoretical prediction	3
<b>Fig. 1.3.</b> Thermotropic LCs exhibit a phase transition into the LC phase as temperature is changed.	4
<b>Fig. 1.4.</b> The three types of deformation occurring in nematics. The figure shows how each type may be obtained separately by suitable glass walls.	5
<b>Fig. 1.5.</b> The angle, $\theta$ , between the director of LC molecules and the propagation direction of incident light will affect the effective index of extraordinary wave.	6
<b>Fig. 2.1.</b> LT-GaAs PC antenna	11
<b>Fig. 2.2.</b> Schematic diagram of the transmission-type THz-TDS system.	12
<b>Fig. 2.3.</b> The results of the THz signal passing through the air. (a) and (b) are time domain waveforms with and without purge; (c) and (d) are frequency domain spectrum with and without purge, respectively.	14
<b>Fig. 2.4.</b> THz detector.	16
<b>Fig. 2.5.</b> The sketches of reference cell (a) and the LC cell (b).	19
<b>Fig. 3.1.</b> A six-stage folded Solc filter	28
<b>Fig. 3.2.</b> The light path mechanism after passing six half wave plates.	28
<b>Fig. 3.3.</b> Schematic diagram of the LC-based tunable THz Solc filter. The inset (a) and (b) show two different ways to apply magnetic field on the same tunable LC THz retarders, respectively.	32

**Fig. 3.4.** Experimental setup of the LC-based tunable THz Solc filter. The Fig. (a) and (b) refer to the schematic diagram in Fig. 3.3 (a) and (b), respectively. **33**

**Fig. 3.5.** An example of the transmittance of the broadband THz pulse through LC Solc filter filled with E7. The circles are experimental data and the solid line is theoretical prediction. **35**

**Fig. 3.6.** An example of the transmitted spectrum of the broadband THz pulse which is tuned using a LC (E7) THz Solc filter. The insert is time domain profiles. The circles and squares are experimental data and the solid lines are the theoretical prediction. **36**

**Fig. 3.7.** The first-order central frequencies of the filter filled with E7 versus rotation angle  $\theta$  between magnetic field and z axis. The circles are experimental data. The curve is theoretical calculation. **37**

**Fig. 3.8.** An example of the transmitted spectrum of the broadband THz pulse through LC Solc filter filled DN125262W. The circles are experimental data and the solid line is theoretical prediction. **38**

**Fig. 3.9.** The central transmitted frequencies of the filter filled with DN125262W versus rotation angle  $\theta$  between magnetic field and z axis. The circles are experimental data. The curve is theoretical. **38**

**Fig. 3.10.** The temporal profiles of a THz pulse through (a) E7 based Solc filter and reference LC cells (b) DN125262W based Solc filter and reference ones. **40**

**Fig. 4.1.** The simulation results of electric field distribution between electrodes in an empty LC cell (a) in a lateral view (b) in a top view. **46**

**Fig. 4.2.** The schematic diagram of homeotropical alignment LC cell. The cell gap is 1.5mm. **47**

**Fig. 4.3.** The schematic diagram of one element in a tunable LC THz Solc filter. The propagation direction of the THz wave is along Z axis. The direction of applied electrical field is tilted with  $22.5^\circ$  or  $-22.5^\circ$  referring to X axis. **47**

**Fig. 4.4.** The experimental picture of the two folded THz Solc filter based on LCs. **48**

**Fig. 4.5.** The schematic diagram of LC molecules orientating under different fields.  $E_c$  is the threshold voltage and  $E$  is the applied field. **49**

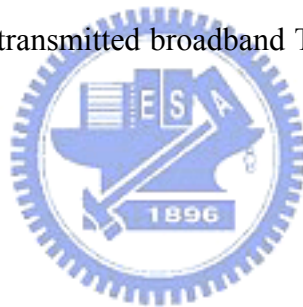
**Fig. 4.6** Spectra of the transmitted broadband THz pulse through the LC THz Solc filter at several voltages. The circles, diamonds and squares are experimental data and the solid lines are the theoretical prediction. **51**

**Fig. 4.7.** The central transmitted frequencies of the filter versus applied voltages. The circles are experimental data. The curve is theoretical line. **52**

**Fig. 4.8.** Solc filters consist of wave plates of two thicknesses. The circles and squares are experimental data. The curves are theoretical prediction. **53**

**Fig. 4.9.** The schematic diagram of a tunable four folded cascaded THz Solc filter. **54**

**Fig. 4.10.** Spectra of the transmitted broadband THz pulse through the four folded Solc filter at two voltages. **55**



# Chapter1. Introduction

In these twenty years, resplendent progress in terahertz (THz) wave field has been made. THz frequency locates between microwave and visible which is shown in Fig. 1.1. The development of solid-state femtosecond lasers and advanced optoelectronic THz-devices promote a new era of fundamental and applicable THz science. THz studies ranging from investigations of ultrafast dynamics in materials to biological media and three dimensional imaging have been actively explored. For today and future applications in THz science, quasi-optic components such as filters are indispensable.

However, there are shortages of optical components in the THz frequency range. Most THz tunable devices such as filters have the problems with small tunable range and cryogenic operating temperature. More recently, we have demonstrated the both electrically and magnetically controlled liquid-crystal (LC) THz phase shifter [1,2]. Here, we propose to study and design the THz Solc filter by using LC retarders. The purpose is to solve the current lack of the THz wavelength filter with large tunable range.

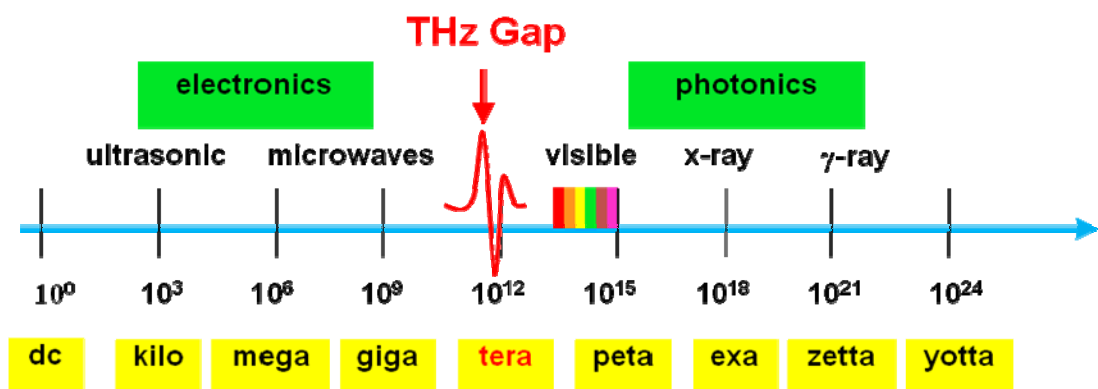


Fig. 1.1. The diagram defines the name of electromagnetic wave in different frequency ranges. (Modification from X.-C.Zhang, published in 2005)

In this chapter, the background information on our recently survey of THz Filter, and the background information of Nematic LCs (NLCs) are presented. The structure of the thesis is presented in the last part of this chapter as “Thesis highlight”.

## 1.1 Terahertz technology: Terahertz Filter

Ultrafast optoelectronic technology has been developed for these decades, and many applications of THz spectroscopy are exploited. Many quasi-optic components such as phase shifters, attenuators, polarizers, and filters are in high demand. Recently, several types of tunable THz filters have also been demonstrated. These include: a tunable THz attenuator and filter (operating at cryogenic temperature) based on a mixed type-I/type-II GaAs/AlAs multiple quantum well structure tuned by optical injection [3]; by using of SrTiO<sub>3</sub> as a defect material inserted into a periodic structure of alternating layers of quartz and high-permittivity ceramic, a photonic crystal filter tuned from 185 GHz at 300 K down to 100 GHz at 100 K [4]; some groups using voltage controlled wavelength selection at microwave frequencies by zero-order grating with LCs [5]; a metallic hole arrays or photonic crystals (MHA or MPC) filter made tunable over the range of 365-386 GHz by a relative lateral shift of 140 μm between two micro-machined MPC plates [6], control of enhanced THz transmission through two dimensional MHA using magnetically controlled birefringence in NLCs [7] and a magnetically controlled LC based THz tunable Lyot filter with tunable range from 0.388 to 0.564 THz [8].

The magnetically controlled LC based THz tunable Lyot filter was demonstrated and published in Applied Physics Letters in March 2006 by our group

previously. This filter is the first time a tunable room-temperature THz filter. Fig. 1.2 (a) and (b) are the experimental arrangement and the peak transmitted frequencies of Lyot filter vs different time delay,  $\Delta\tau_A$ . However, considering practicability and functionality, we demonstrate a THz tunable Solc filter in this thesis.

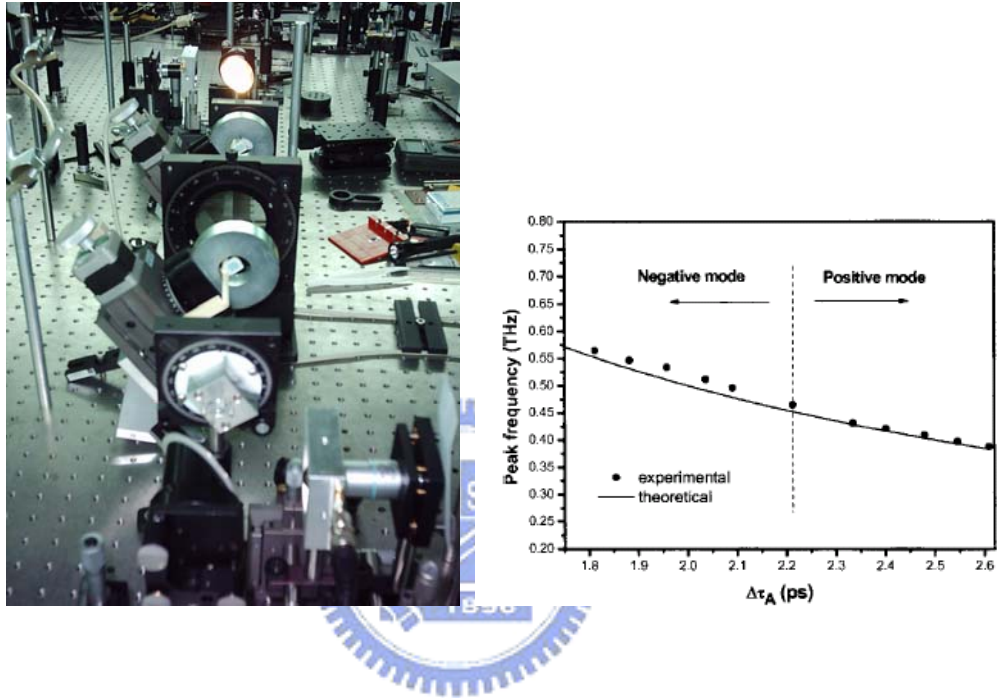


**Fig. 1.2. (a) The experimental diagram of the LC-based tunable THz Lyot filter. (b) The peak transmitted frequencies of the filter vs different time delay,  $\Delta\tau_A$ . The circles are experimental data and the curve is theoretical prediction.**

## 1.2 Nematic Liquid Crystal

The first observation of liquid crystalline or meso-morphic behavior was made near the end of 19th century by Reinitzer and Lehmann [9, 10]. LCs are substances that exhibit a phase of matter with properties between a conventional liquid, and a solid crystal. Therefore, a LC may flow like a liquid, but has the molecules in the liquid oriented in a crystal-like way. There are many different types of LC phases,

which can be distinguished based on their different optical properties (such as birefringence). LCs can be divided into thermotropic and lyotropic LCs. Thermotropic LCs exhibit phase transition into the LC phase as temperature is changed (Fig. 1.3), whereas lyotropic LCs exhibit phase transition as a function of concentration of the mesogen in a solvent (typically water) as well as temperature.

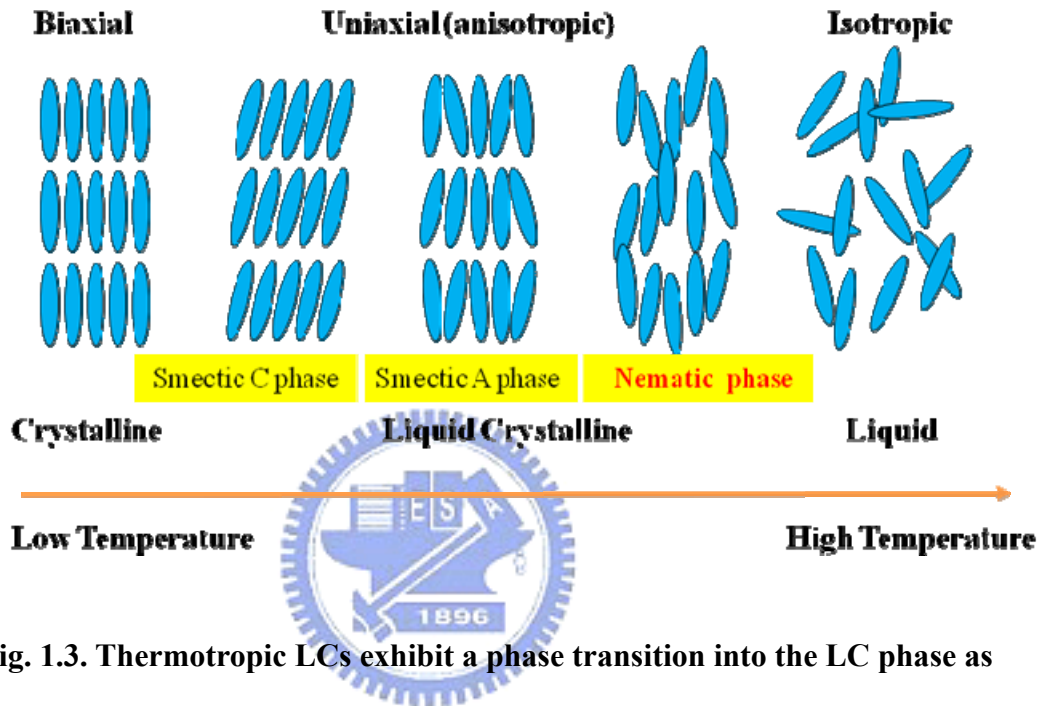


**Fig. 1.3. Thermotropic LCs exhibit a phase transition into the LC phase as temperature is changed.**

Thermotropic LCs includes smectic phase, nematic phase, chiral phase, and discotic phases. However, nematic phase is most common investigated; the LCs utilized in our work is all rod-like nematic LCs, where the molecules have no positional order, but they have long-range orientational order. Most nematics are uniaxial: they have one axis labeled as a unit vector (or director), with the other two being equivalent (can be approximated as cylinders). Some LCs are biaxial nematics, meaning that in addition to orienting their long axis, they also orient along a secondary axis.

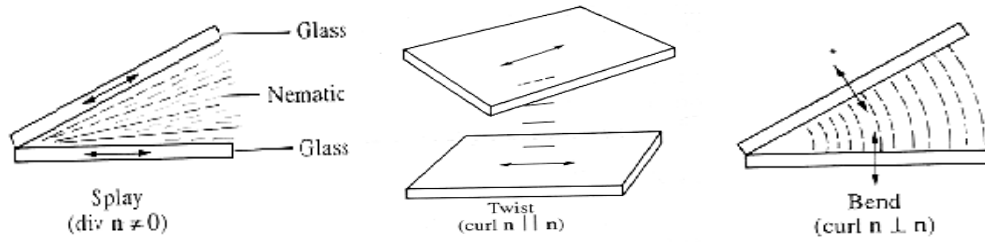


**Fig. 1.4. The three types of deformation occurring in nematics. The figure shows how each type may be obtained separately by suitable glass walls. (Reproduced from P. G. de Gennes and J. Prost, *The Physics of Liquid Crystals*, 2nd ed. , Oxford, New York, 1983).**

We also can use some boundary conditions, add chiral dopant, or apply external field (magnetic or electrical field) to rearrange LC molecules. For a uniaxial system, single crystal, the molecules along one common direction  $\pm \hat{n}$  in an ideal. Three types of the deformation (splay, twist, and bend) occur in nematic phase as shown in Fig. 1.4 [11]. Briefly, the LC molecules tend to orient parallel or perpendicular to the external field and the extra energy density is a function of the direction and magnitude of the field. Besides, the LC molecules around a strong boundary condition will be aligned and twisted due to the lowest total energy.

As mentioned above, nematic LC molecules tend to be parallel to the director composing an optically uniaxial system where the refractive index is birefringence. The ordinary index  $n_o$  is for light with polarization perpendicular to the director, whereas the extraordinary index  $n_e$  is for light with polarization parallel to the director. The birefringence of nematic LCs is defined as [12]

$$\Delta n = n_{eff} - n_o \tag{1.1}$$



If the incident polarization of light has tilt angle with respect to the director, the refractive index of extraordinary wave should be rewritten as:

$$n_{eff} = \left( \frac{\sin^2 \theta}{n_{//}^2} + \frac{\cos^2 \theta}{n_{\perp}^2} \right)^{-\frac{1}{2}} \quad (1.2)$$

where  $\theta$  is the angle between the propagation direction of incident light and the optical axis as shown in Fig. 1.5.

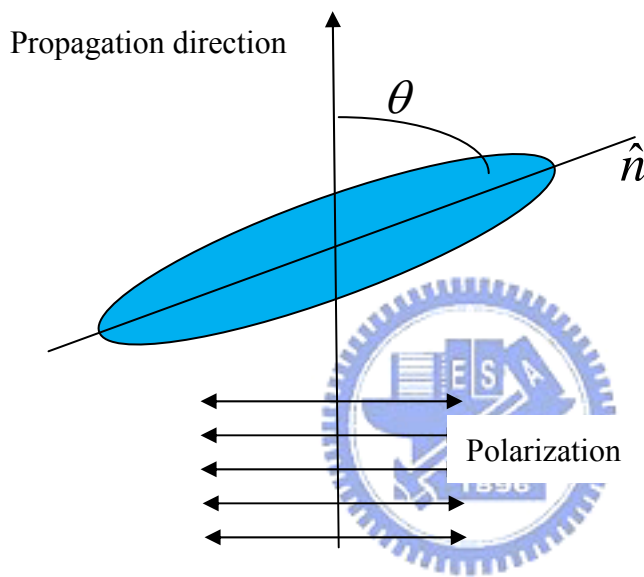


**Fig. 1.5. The angle,  $\theta$ , between the director of LC molecules and the propagation direction of incident light will affect the effective index of extraordinary wave.**

### 1.3. Thesis highlights

In chapter 2, we depict the schematic setup of THz Time Domain Spectroscopy (THz-TDS) radiation using photoconductive (PC) antenna, and explain the generation and detection principles of THz-TDS radiation with PC antenna. Then, the characteristics of radiation and detection in our TDS system are discussed.

Finally, we extracted the refractive index of E7 (Merck) and a new LC: DN125262W

(daily polymer corporation) in THz range via THz-TDS system.

In chapter 3 and 4, a magnetically controlled LC-based THz tunable Solc filter and an electrically controlled LC-based THz tunable Solc filter have been reported, respectively. We design various structures of the LC based filter to get extensive applications in THz range. Finally, we give a conclusion in chapter 5.



## 1.4. References:

1. C.Y. Chen, C.F. Hsieh, Y.F. Lin, R.P. Pan, and C.L. Pan, Magnetically tunable room-temperature  $2\pi$  liquid crystal Terahertz phase shifter., Opt. Express, **12**, 2630-2635 (2004).
2. C.F. Hsieh and R.P. pan, T.T. Tang, H.L. Chen, and C.L. pan, "Voltage-contralled liquid-crystal terahertz phase shifter and quarter-wave plate," Opt. Lett., **31**,1112-1114 (2006).
3. I. H. Libon, S. Baumgärtner, M. Hempel, N. E. Hecker, J. Feldmann, M. Koch, and P. Dawson, "An optically controllable terahertz filter," Appl. Phys. Lett. **76**, 2821-2823 (2000).
4. H. Nemeč, P. Kuzel, L. Duvillaret, A. Pashkin, M. Dressel, M. T. Sebastian, " Highly tunable photonic crystal filter for the terahertz range," Opt. Lett., **30**, 549-551 (2005).
5. F. Yang and J. R. Sambles, "Microwave liquid crystal wavelength selector," Appl. Phys. Lett., **79**, 3717-3719 (2001).
6. T. D. Drysdale, I. S. Gregory, C. Baker, E. H. Linfield, W. R. Tribe, D. R. S. Cumming, "Transmittance of a tunable filter at terahertz frequencies," Appl. Phys. Lett. **85**, 5173-5175 (2004).
7. C.-L. Pan, C.-F. Hsieh, and R.-P. Pan , M. Tanaka, F. Miyamaru, M. Tani, and M. Hangyo, "Control of enhanced THz transmission through metallic hole arrays using nematic liquid crystal," Opt. Express **13**, 3921-3930 (2005).
8. C.-Y. Chen, C.-L. Pan, C.-F. Hsieh,Y.-F. Lin, and R.P. Pan, "Liquid-crystal-based terahertz tunable Lyot filter," Appl. Phys. Lett. **88**, 101107 (2006)
9. R. Reinitzer, "Zur Kenntnis des Cholesterins," Monatsh. Chem. **9**, 421-441 (1888).
10. O. Lehmann, "On flowing crystals," Z. Phys. Chem. **4**, 462 (1889).

11. P. G. de Gennes and J. Prost, *The Physics of Liquid Crystals*, **2<sup>nd</sup> ed.** (Oxford, New York, 1983).

12. For example, Eugene Hecht, *Optics*, **3<sup>rd</sup> ed.** (John Wiley & Sons, New York, 1999).



# Chapter2. Terahertz

## Time-domain-spectroscopy (THz-TDS)

### 2.1. Introduction

Investigations of LC filters in the THz frequency range utilized THz time domain spectroscopy (THz-TDS). THz-TDS is a powerful technique allowing broadband THz generation and detection of field amplitude and phase. Various techniques is used to generate THz radiation, such as ultrafast switching of photoconductive antennas [1], rapid screening of the surface field via photoexcitation of dense electron hole plasma in semiconductors[2], rectification of optical pulses in crystals[3], and carrier tunneling in coupled double-quantum well structures[4]. However, photoconductive (PC) antennas have a promising source of intensity and spectral bandwidth.

Therefore, in this chapter we discuss photoconductive emitter and detector antennas in THz-TDS system in Sec.2.2 and deduce the generation and detection principles of photoconductive antennas in Sec.2.3 and Sec.2.4. Finally, we extract the refractive index of a large birefringence LC-DN125262W by using THz-TDS system in Sec.2.5.

### 2.2. Schematic setup of THz-TDS radiation using PC antenna

Low –temperature grown GaAs (LT-GaAs) was used as the PC substrate for generation and detection of THz waves. The material has great advantages of short

carrier life time, reasonably high mobility, and high break down electrical field. A PC antenna with a pair of square stab at the center of a coplanar transmission line on LT-GaAs was used for an emitter and a detector (Fig. 2.1).

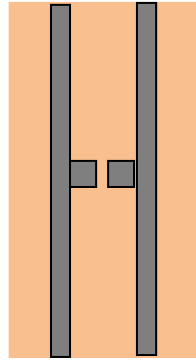
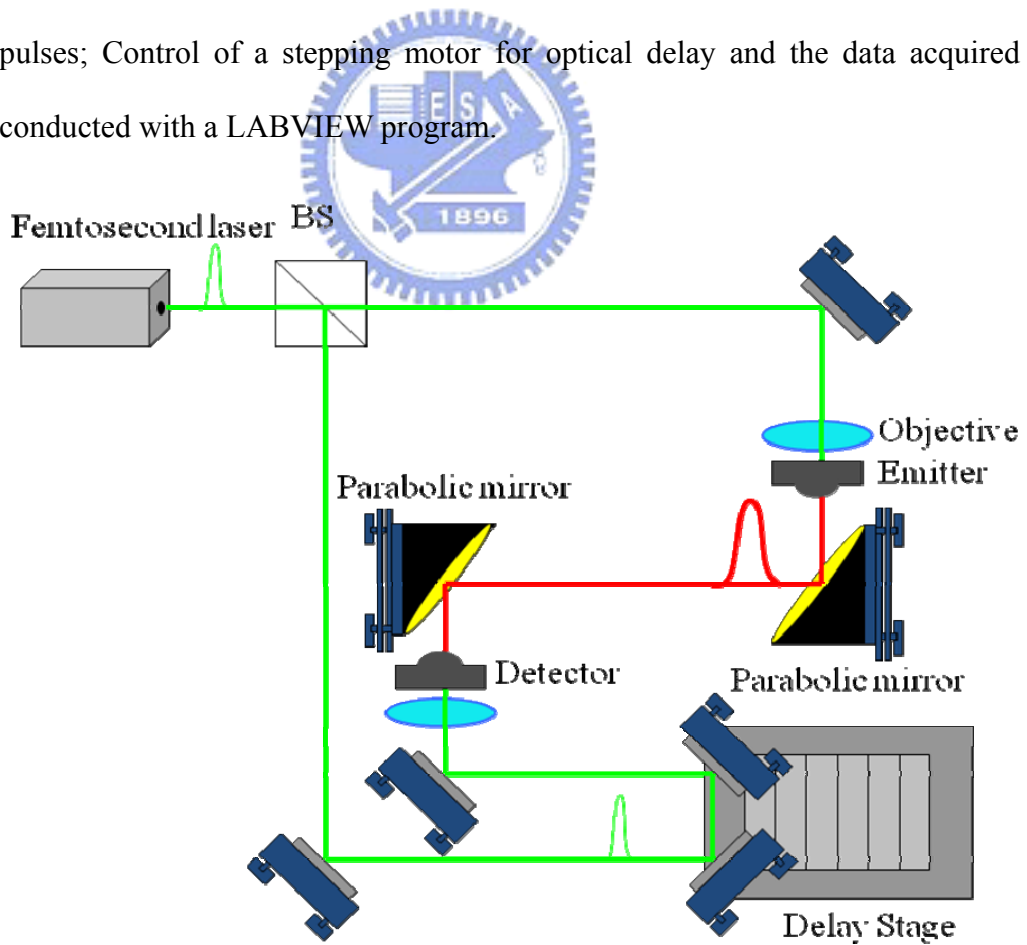


**Fig. 2.1. LT-GaAs PC antenna**

A mode-locked Ti: sapphire laser (Spectra Physics Tsunami) is the light source to excite PC antennas. The pulse width and the repetition rate of the laser were 50 fs and 82 MHz, respectively. The pulses are split into two beams: one is the so-called pump or excited beam; the other is referred as the probe beam. A schematic representation of our system is depicted in Fig. 2.2. Pump pulse were focused on the biased gap of the dipole-type LT-GaAs PC antenna, which results in conductivity in the gap varying in subpicosecond time scale.

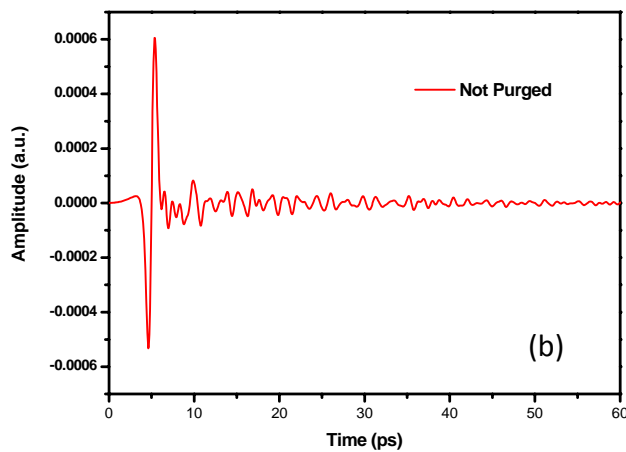
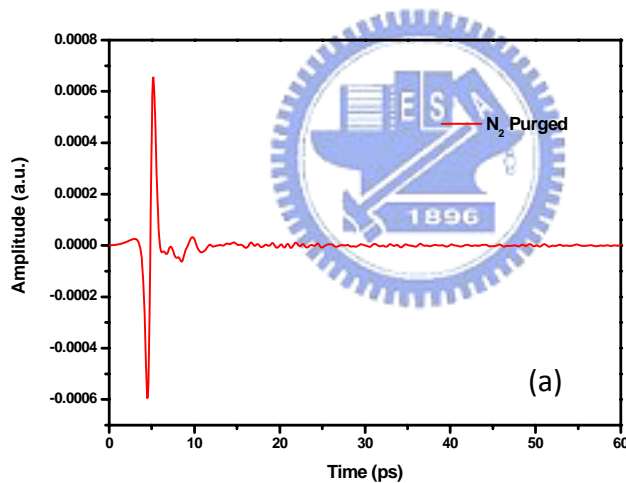
The transient variation of conductivity caused the transient electrical current in the gap, leading to generation of THz radiation. Average power of pump pulse is about 35 mW and 5 volt is applied to the coplanar transmission line. A hemispherical silicon substrate lens attached to the antenna to avoid the multiple reflections within the SI-GaAs substrate. The generated THz pulses are collected and guided by a pair of gold-coated parabolic mirrors. The incident THz waves on the sample can be focused by one parabolic mirror. The transmitted waves from the sample are focused

by another parabolic mirror onto the detector of dipole-type LT-GaAs PC antenna also attached a hemispherical silicon substrate lens. The Ti:sapphire laser probe pulse impinged on LT-GaAs generating charge carriers and effectively turned on the antenna for a short time interval. Average power of probe pulse is 15mW and time interval typically is a few hundreds of femtoseconds determined by the lifetime of the excited carriers. Transient current was induced in the gap of the detector antenna with the focused THz electric field, which accelerated the photocarriers excited by the probed beam. PC current signal, with 5 kHz-modulation of the bias applied to emitter, was synchronously detected by a digital lock-in amplifier equipped with a current-voltage preamplifier module (Stanford Research Systems, Model SR830). The transmitted THz pulse was monitored by scanning the optical delay of the probe pulses; Control of a stepping motor for optical delay and the data acquired were conducted with a LABVIEW program.



**Fig. 2.2. Schematic diagram of the transmission-type THz-TDS system.**

The diameter of the THz beam was  $\sim 8$  mm, the total scanning duration of the THz was 68 ps, and the measurements were done at room temperature ( $25\pm 0.5^\circ\text{C}$ ). Fig. 2.3 is the results of the THz signal passing through the air with purge and without purge. Apparently, the pulse after main signal is smooth in purge condition while the pulse after main signal fluctuates severely in no purge condition due to water absorption referring to Fig. 2.3 (a) & (b). As to frequency domain, the spectrum in Fig. 2.3 (d) has many absorption lines of water below 2 THz, comparing with the spectrum in Fig. 2.3 (b). Besides, the power spectrum extends to 2THz and its the signal/noise is up to  $10^7$ , which is a well performance system to measure many characteristics of devices.





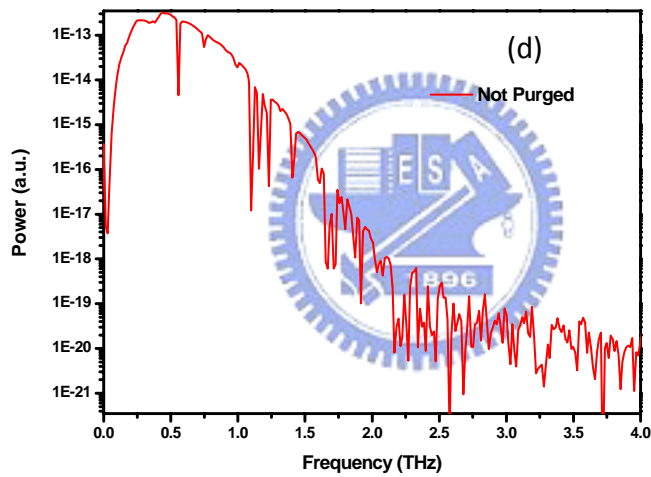
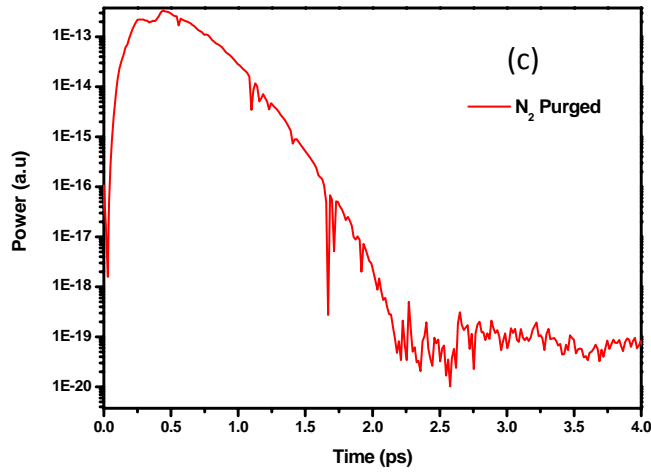


**Fig. 2.3.** The results of the THz signal passing through the air. (a) and (b) are time domain waveforms with and without purge; (c) and (d) are frequency domain spectrum with and without purge, respectively.

### **2.3. Generation of THz radiation Using PC antenna**

When a biased semiconductor is pumped by an ultrafast laser pulse, the rapid change of the transport photocurrent gives rise to electromagnetic radiation. The following calculation is based on Drude-Lorentz theory of carrier transports in

semiconductors [5]. When the carrier is pumped by ultrashort laser pulse, the time dependence of carrier density is given by:

$$\frac{dn}{dt} = -\frac{n}{\tau_c} + G \quad (2.1)$$

where  $n$  is the density of the carrier,  $G$  is the generation rate of the carrier by the laser pulse, and  $\tau_c$  is the carrier trapping time.

Again, the generated carriers can be accelerated in biased electrical field. The acceleration of carriers is given by:

$$\frac{dv_{e,h}}{dt} = -\frac{v_{e,h}}{\tau_s} + \frac{q_{e,h}}{m_{e,h}} E \quad (2.2)$$

where  $v_{e,h}$  is the average velocity of the carrier,  $q_{e,h}$  is the charge of an electron (a hole),  $m_{e,h}$  is the effective mass of an electron (a hole),  $\tau_s$  is the momentum relaxation time, and  $E$  is the local electrical field, which is less than the applied bias  $E_b$  due to the screen effect of space charges. More precisely,

$$E = E_b - \frac{P}{\alpha \epsilon} \quad (2.3)$$

where  $P$  is the polarization induced by the spatial separation of the electron and hole,  $\epsilon$  is the dielectric constant of the substrate, and  $\alpha$  is the geometrical factor of photoconductive material, which is equal to three in isotropic dielectric material.

The time dependence of polarization  $P$  can be written by:

$$\frac{dP}{dt} = -\frac{P}{\tau_r} + J \quad (2.4)$$

where  $\tau_r$  is the recombination time between an electron ( $\tau_r = 10$  ps for LT-GaAs) and a hole and  $J = env_h - env_e$  is the current density.

In short, according to Hertzian dipole theory, the far-field radiation is given by:

$$E_{THz} \propto \frac{\partial J}{\partial t} \propto ev \frac{\partial n}{\partial t} + en \frac{\partial v}{\partial t} \quad (2.5)$$

where  $v = v_h - v_e$  is a relative speed  $v$  between an electron and a hole

Therefore, the transient electromagnetic field  $E_{THz}$  is composed of two parts: one is due to carrier acceleration under the electric field, and the other is due to the change of carrier density.

## 2.4. Detection of THz-TDS radiation using PC antenna

For the detection of THz field, which is a Gaussian beam on the detector expressed as [6]:

$$E(x, y) = E_0 \exp\left[-\frac{(x^2 + y^2)}{w_1^2}\right] \quad (2.6)$$

where  $w_1$  is the spot size.

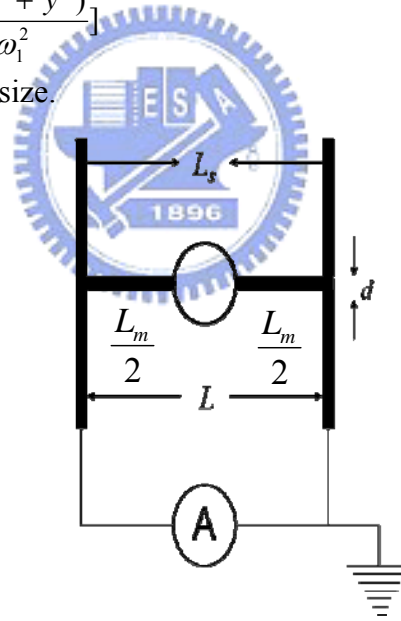


**Fig. 2.4. THz detector.**

The total resistance over the detector is:

$$R = \frac{\rho_M L_M + \rho_s L_S}{td} \approx \frac{\rho_s L_S}{td} \quad (2.7)$$

where  $L_M$  is the total length of the metal electrodes,  $L_S$  is the length of the switch area between the two electrodes tips,  $\rho_M$  and  $\rho_s$  are their resistivity,

respectively, and  $d$  is the width of electrode and the gap area as shown in Fig. 2.4. The average resistivity  $\rho_s$  is larger than  $\rho_M$  due to the low duty cycle of the driving laser (100 fs/10 ns =  $10^{-5}$ ). The resistivity  $\rho_s$  depends on photogenerated carrier density, which for homogeneous illumination of power  $P_{laser}$  scales as:

$$\rho_s = \frac{L_s d}{\xi P_{laser}} \quad (2.8)$$

where  $\xi$  is a conversion factor between laser power and number of photogenerated carriers.

The average electric field  $\bar{E}$  across the detector gives rise to a potential difference  $U = \bar{E}(L_M + L_S)$ , so the average current is

$$I = \frac{U}{R} = \frac{\bar{E}(L_M + L_S)}{L_S^2} t d \xi P_{laser} \quad (2.9)$$

The average electric field across the detector area is

$$\overline{E(L, d)} = \frac{1}{Ld} \int_{-\frac{L}{2}}^{\frac{L}{2}} \int_{-\frac{d}{2}}^{\frac{d}{2}} E(x, y) dx dy = \frac{E_0 \pi \omega_1^2}{Ld} \text{Erf}\left(\frac{L}{2\omega_1}\right) \text{Erf}\left(\frac{d}{2\omega_1}\right) \quad (2.10)$$

where  $\text{Erf}(\chi) = \left(\frac{2}{\pi}\right) \int_0^\chi \exp(-u^2) du$  is an error function. The peak strength of the electric field,  $E_0$ , can be expressed in terms of the total power of THz beam:

$$P_{THz} = \frac{1}{2} c \epsilon_0 \int_{-\infty}^{\infty} \int_{-\infty}^{\infty} E^2(x, y) dx dy = \frac{1}{2} \pi \omega_1^2 c \epsilon_0 E_0^2 \quad (2.11)$$

$$\Rightarrow E_0^2 = \frac{2}{\omega_1} \sqrt{\frac{P_{THz}}{\pi c \epsilon_0}} \quad (2.12)$$

Besides, for wavelength  $\lambda \ll \frac{\pi \omega_0^2}{R_L}$ , however, the lens is cut to place the detector

$$\text{gap at the position given by } h = R_L \frac{n}{n-1} \quad (2.13)$$

where  $R_L$  is the lens radius and  $n$  is the index of refraction of the lens material.

Justifying the lens design:

$$\lim_{\lambda \rightarrow 0} d_{focus} = R_L \frac{n}{n-1}$$

$$\lim_{\lambda \rightarrow 0} \omega_1(d_{focus}) = \frac{\lambda}{\pi\omega_0} \frac{R_L}{n-1} = \frac{c}{\pi\nu\omega_0} \frac{R_L}{n-1} \quad (2.14)$$

Where  $\nu = \frac{c}{\lambda}$  is the frequency.

By inserting Eq. (2.12), together with Eq. (2.14), into the expression for the detector current, Eq. (2.9), we get

$$I(\nu) = \xi P_{laser} \sqrt{\frac{cP_{Thz}}{\pi\epsilon_0}} \frac{2R_L t}{L_S^2 d\omega_0 (n-1)} \frac{1}{\nu} \text{Erf} \left[ \frac{L (n-1)\pi\omega_0}{2 cR_L} \nu \right] \text{Erf} \left[ \frac{d (n-1)\pi\omega_0}{2 cR_L} \nu \right] \quad (2.15)$$

In short, the time domain signal  $I(\nu)$  relative to the emitted THz electric field  $E$  and the response function of the detector. The carrier life time of LT-GaAs, transmission characteristics of the SI-GaAs substrate and LT-GaAs film, resonance characteristics of dipole-type antenna, diffraction effect of the THz beam optics, and pulse widths of probe beam, etc, all contribute to the transient response function of the detector.

## 2.5. The application of THz-TDS system: extracting the refractive index of a large birefringence LC-DN125262W

The knowledge of the frequency dependence and the magnitude of the refractive indices as well as the birefringence of liquid crystal is a key parameter for practical applications of LCs. Although many groups have investigated the birefringence of LCs in visible or infrared range, we expect a large birefringence with low loss LCs in THz range.

For searching high birefringence LCs, we measure the refractive index of a large birefringence LC\_DN125262W, a special mixture from daily polymer corporation, by using THz-TDS to determine it. We prepared two cells: the reference cell is constructed by two fused silica substrates contacting each other; each LC cell is constructed by two fused silica substrates separated by an aluminum spacer and filled with DN125262W as shown in Fig 2.5. The inner surfaces are coated with polyimide films, which are baked and rubbed to give LCs the homogeneous alignment.

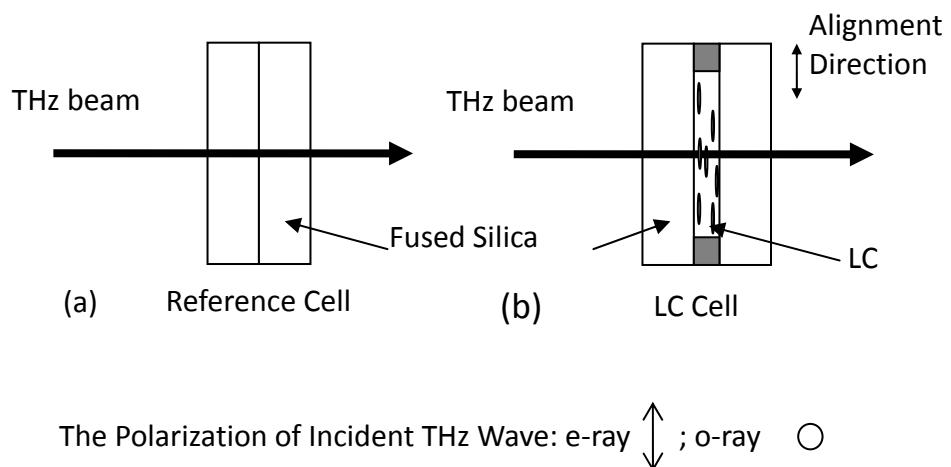


**Fig. 2.5. The sketches of reference cell (a) and the LC cell (b).**

If a plane wave pass through the cell normally, the electric field of the THz wave through the reference cell at angular frequency,  $\omega$ , can be written as

$$E_{reference}(\omega) = E_0(\omega) \cdot \eta(\omega) \cdot P_{air}(\omega, d) \quad (2.16)$$

where  $E_0(\omega)$  is the electric field of THz wave before passing through the cell,  $\eta(\omega)$  is a coefficient including all the reflection, transmission and propagation coefficients in fused silica and  $P_{air}(\omega, d)$  is the propagation coefficient in air, which  $d$  is the thickness of the LC layer. Generally, for a medium over a distance  $L$ , the propagation coefficient  $P_a(\omega, L)$  can be written as  $\exp[(-i\tilde{n}_a\omega L)/c]$ , where  $\tilde{n}_a$  ( $=n_a - i\kappa$ ) is the complex refractive index of medium a, which depends on the wave frequency. In  $\eta(\omega)$ , the echoes of the THz wave or Fabry-Perot effect in fused silica can be neglected since in the thick sample, these echoes are far away from the main signal on the time domain and can be truncated during the spectrum analysis. The electric field of a THz wave passing through the LC cell is given by:

$$E_{LC}(\omega) = E_0(\omega) \cdot \eta(\omega) \cdot T_{q-LC}(\omega) \cdot P_{LC}(\omega, d) \cdot T_{LC-q}(\omega) \cdot F_{LC}(\omega, d) \quad (2.17)$$

where  $T_{i-j}(\omega)$  is the transmitted Fresnel factor of  $i - j$  interface, which is

$T_{i-j}(\omega) = (2 \cdot \tilde{n}_i) / (\tilde{n}_i + \tilde{n}_j)$  and  $F_a(\omega, L)$  is the Fabry-Perot effect in a medium with thickness  $L$ . Because of the same thickness of fused silica substrates used in this work,  $\eta(\omega)$  is equal to the reference cell. The complex transmission coefficient  $T(\omega)$  of the measured LC as follow:

$$T(\omega) = \frac{E_{LC}(\omega)}{E_{ref}(\omega)} = \frac{4 \cdot \tilde{n}_{LC} \cdot \tilde{n}_q}{(\tilde{n}_{LC} + \tilde{n}_q)^2} \cdot \exp[-i(\tilde{n}_{LC} - \tilde{n}_{air}) \frac{\omega \cdot d}{c}] \cdot F_{LC}(\omega) \quad (2.18)$$

where  $\tilde{n}_q$  is the complex index of fused silica and  $\tilde{n}_{LC}$  is the ordinary index  $\tilde{n}_o = n_a - i\kappa_o$  or extraordinary index  $\tilde{n}_e = n_e - i\kappa_e$ . Duvillaret et al. have

demonstrated the solutions in 1996 for optically thick and thin samples [7]. Here, we make thick sample to simplify the analysis processes such that the echoes of THz waves from multiple reflections of sample are temporally well separated from main signal. So  $F_{LC}(\omega)$  in Eq. 2.18 can be equal to 1.

If we let the reference cell have an empty gap of the same thickness of LC cell, the  $F(\omega)$  will be rewritten as

$$F_{LC}(\omega) = \frac{(\tilde{n}_q - \tilde{n}_{air}) \cdot (\tilde{n}_{air} - \tilde{n}_q) \cdot (\tilde{n}_{LC} + \tilde{n}_q) \cdot \exp\left(\frac{2i(\tilde{n}_{LC} - \tilde{n}_{air})\omega d}{c}\right)}{(\tilde{n}_q - \tilde{n}_{LC}) \cdot (\tilde{n}_{LC} - \tilde{n}_q) \cdot (\tilde{n}_{air} + \tilde{n}_q)} \quad (2.19)$$

Instead of solving  $\tilde{n}_{LC}$  from  $T(\omega) - T_{meas}(\omega) = 0$ , where  $T(\omega)$  and  $T_{meas}(\omega)$  are respectively the calculated and measured complex transmission coefficients, we define an error function,  $\delta(n, \kappa)$ , and then find  $(n, \kappa)$  by minimizing the error function. The error function is defined as :

$$\delta(n, \kappa) = \delta\rho^2 + \delta\varphi^2 \quad (2.20)$$

$$\text{where } \delta = \ln(|T(\omega)|) - \ln(|T_{meas}(\omega)|) \quad (2.20a)$$

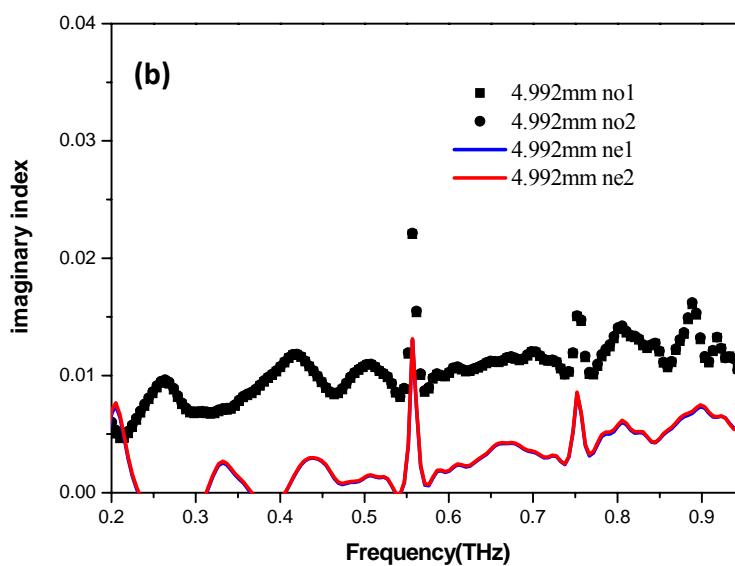
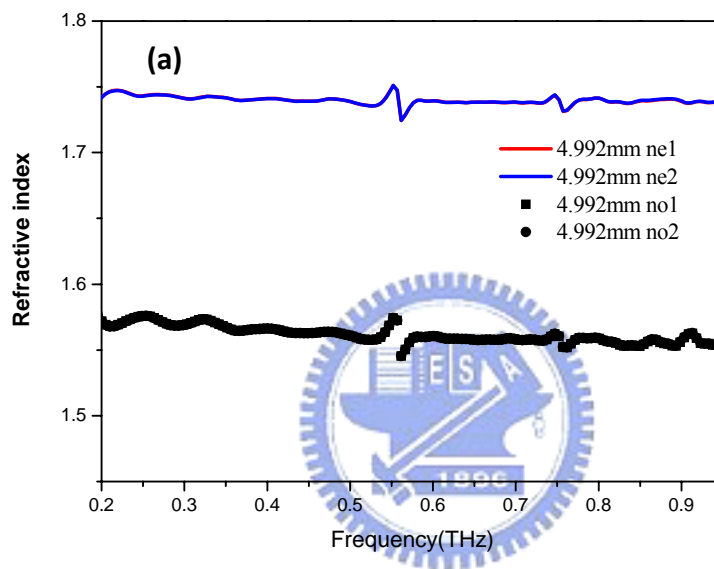
$$\delta\varphi = \arg(T(\omega)) - \arg(T_{meas}(\omega)) \quad (2.20b)$$

After several iterations to minimize the error function by computer programs, we get the refractive indices as following results:

We repeated four times of measurements in the LC cell with 4.992 mm cell gap where to get the same result in each one. Fig. 2.6 (a) is the result of extraordinary and ordinary refractive indices, and (b) is the result of imaginary extraordinary and ordinary refractive indices of DN125262W with 4.992mm cell gap. Besides, we also fabricated DN125262W LC cells with 0.565mm cell gap, and Fig. 2.6 (c) is extraordinary and ordinary refractive indices, and (d) is imaginary extraordinary and



ordinary refractive indices, shown as a function of frequency from 0.2 to 0.95 THz. Comparing with the refractive index of E7, Fig. 2.7. (a) and (b) are the refractive indices of E7 with 8mm cell gap, measured by our group before. Therefore, the birefringence of DN125262W is larger than E7, which largely enhances applications to wave plates or filters. Table 2.1 is a comparison of two kinds of LC molecules according to our measurement.



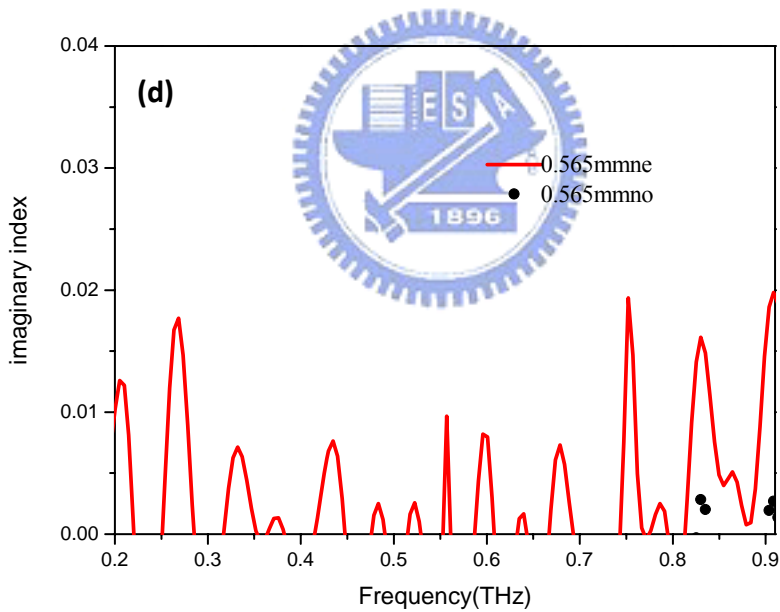
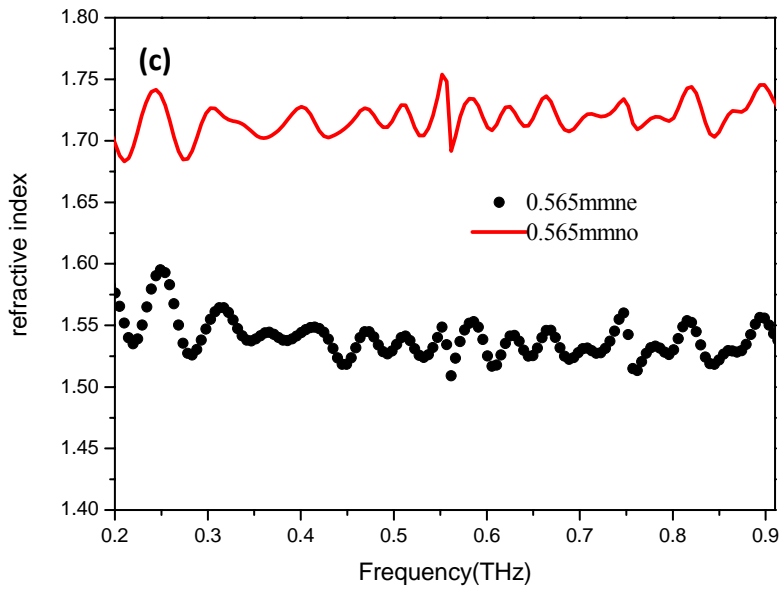


**Fig. 2.6.** The room-temperature (a) extraordinary and ordinary refractive indices, (b) imaginary extraordinary and ordinary refractive indices of DN125262W with 4.992 mm cell gap; (c) extraordinary and ordinary refractive indices, (d) imaginary extraordinary and ordinary refractive indices of DN125262W with 0.565 mm cell gap, are shown as a function of frequency from 0.2 to 0.95 THz.

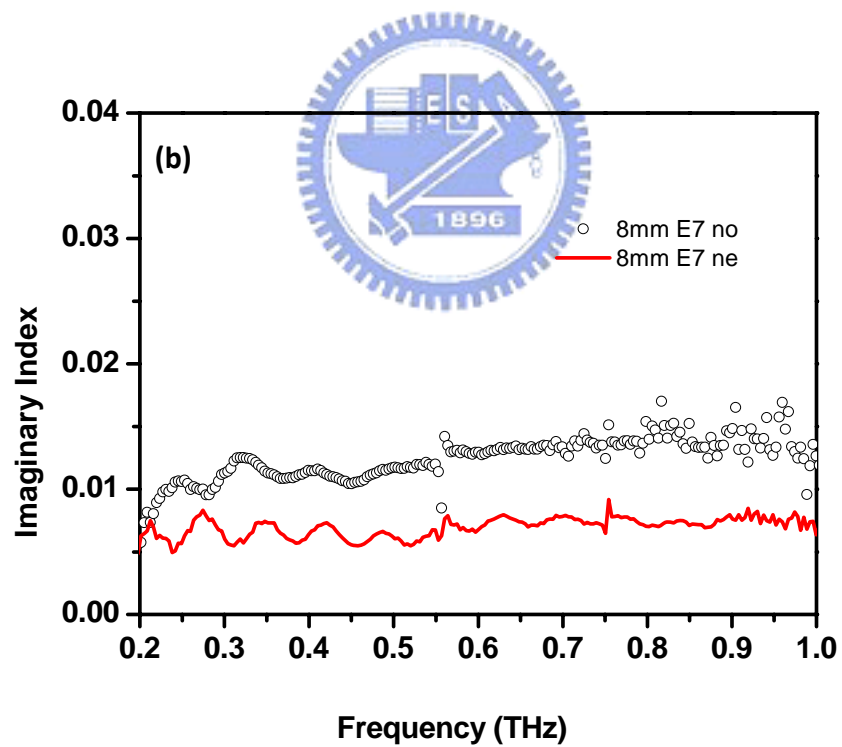
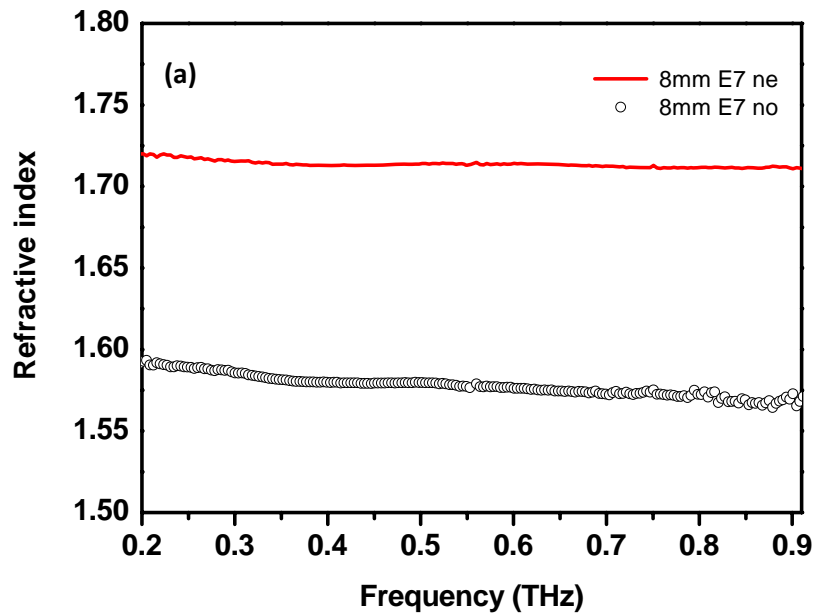
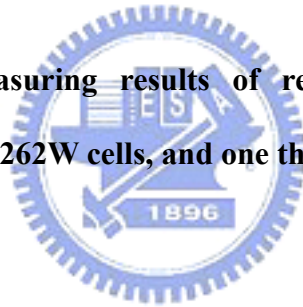


Fig. 2.7. The room-temperature (a) extraordinary and ordinary refractive indices, (b) imaginary extraordinary and ordinary refractive indices of E7 with 8mm cell gap. ( Measured by C.-F. Hsieh)

	<b>E7(8mm)</b>	<b>Large Birefringence LC: DN-125262W (0.565mm)</b>	<b>Large Birefringence LC: DN-125262W (4.992mm)</b>
<b>Ordinary refractive</b>	1.580	1.544	1.566
<b>Extraordinary refractive</b>	1.713	1.728	1.741
<b>Birefringence</b>	<b>0.133</b>	<b>0.184</b>	<b>0.175</b>

**Table 2.1. The measuring results of refractive indices between different thicknesses of DN125262W cells, and one thickness E7 cell.**



## 2.6. References:

1. D. Grischkowsky, S. Keiding, M. van Exter and C. Fattinger: J. Opt. Soc. Am. B **7** (1990) 2006.
2. X.-C. Zhang and D. H. Auston: J. Appl. Phys. **71** (1992) 326.
3. B.B. Hu, X.-C. Zhang, D. H. Auston, and P. R. Smith: Appl. Phys. Lett. **56** (1990) 506.
4. H. G. Roskos, M. C. Nuss, J. Shah, K. Leo, D. A. B. Miller, A. M. Fox, S. Schmitt-Rink and K. Kohler: Phys. Rev. Lett. **68** (1994) 2216.
5. M. Born and E. Wolf: Principles of Optics ( Pergamon, New York, 1959)
6. P. Uhd. Jepsen, R. H. Jacobsen, and S. R. Keiding, "Generation and detection of terahertz pulses from biased semiconductor antennas," J. Opt. Soc. Am. B, Vol. **13**, no. 11, pp. 2424-2436, Nov. 1996
7. L. Duvillaret, F. Garet, and J. Coutaz, "A Reliable Method for Extraction of Material Parameters in Terahertz Time-Domain Spectroscopy," IEEE J. Sel. Top. Quantum Electronics **2**, 739-746 (1996).

# Chapter3. Magnetically Controlled

## Liquid-Crystal-Based Terahertz Tunable

### Solc Filter

#### 3.1. Introduction

Spectral filters can be based on the interference of polarized light. These filters play an important role in many optical systems where filters of extremely narrow bandwidth with wide angular fields or tuning capability are required. In Solar Physics, for example, the distribution of hydrogen may be measured by photographing the solar corona in light of the  $H\alpha$  ( $\lambda = 6563 \text{ \AA}$ ) line. In view of the large amount of light present at neighboring wavelengths, a filter of extremely narrow bandwidth ( $\sim 1 \lambda = \text{\AA}$ ) is required if reasonable discrimination is to be attained. Such filters consist of birefringence crystal plates (wave plates) [1]. The two basic versions of these birefringence filters are Lyot-Ohman filters [2-5] and Solc filters [6, 7]. The Solc filter a type of birefringence filters widely employed in the visible and near infrared, consists of a stack of identical birefringence plates with folded azimuth angles between crossed polarizers or fanned azimuth angles between parallel polarizers. Solc filters can be made tunable using active birefringent retarders such as electro-optic crystals or LC cells. For example, electro-optic Solc-type wavelength filter have been demonstrated in near infrared tuning from 1532.67 to 1529.35nm [8]. In this chapter, we construct and characterize a room-temperature, large tunable-range, THz Solc filter based on magnetically

controlled retardation in LC.

### 3.2. Theory of Solc filter

The folded Solc filter as Fig. 3.1 is composed of a series of even half-wave plates between crossed polarizers and each of wave plates must be oriented at the azimuth angle  $\rho$  and  $-\rho$  alternatively with respect to the polarization of incident electromagnetic wave.

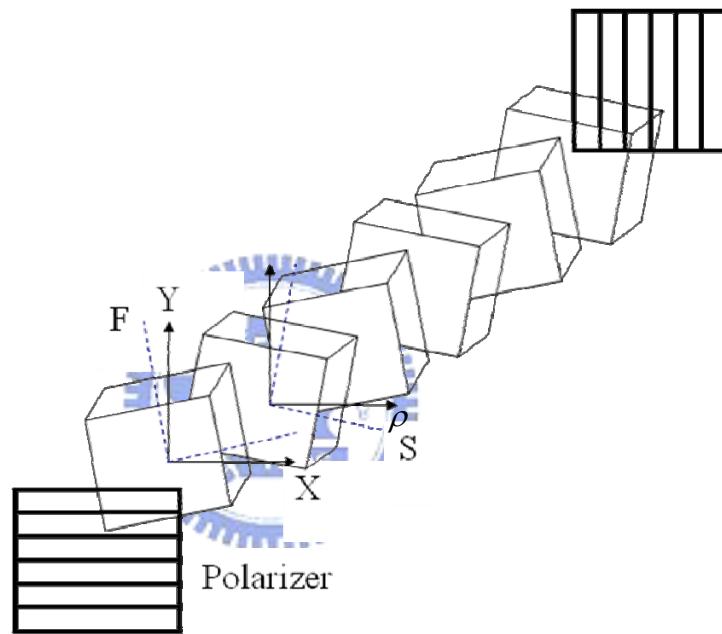


**Fig. 3.1. A six-stage folded Solc filter**

Calculating by Jones matrix formula, the transmittance can be simplified into

$$T = \sin^2 2N\rho. \text{The transmissivity is 100\% if the azimuth angle is equal to } \rho = \frac{\pi}{4N}.$$

The polarization mechanism of light after passing six-stage folded Solc filter can be understood as the picture shown in Fig.3.2.

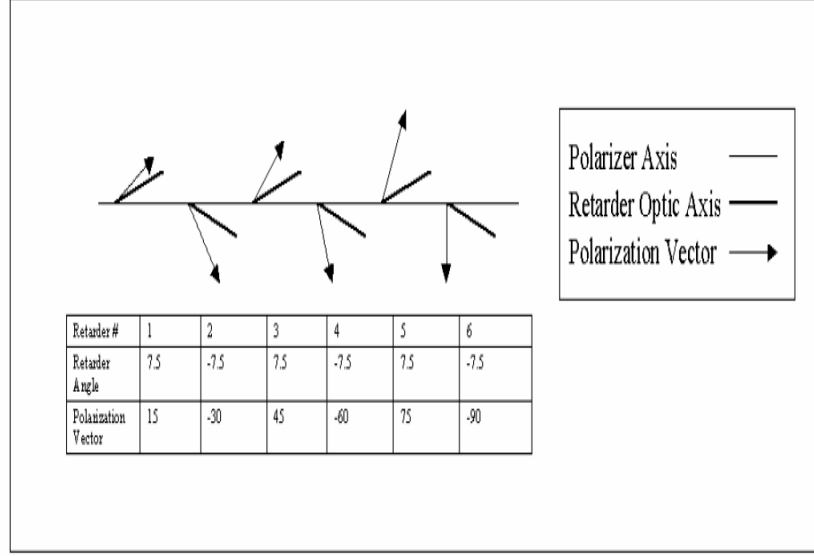


**Fig. 3.2. The light path mechanism after passing six half wave plates.**

According to Fig. 3.2, we can deduce that the final azimuth angle of polarized light after N plates is  $2Np$ . Furthermore, if the final azimuth angle of polarization is equal to  $90^\circ$  at central frequencies, the light passes through the rear polarizer without any loss of intensity but light at other frequencies will have losses. The central frequency  $f_c$  is given by:

$$f_c = \frac{(2m + 1)c}{2(n_e - n_o)d}, m = 0, 1, 2, 3, \dots, \quad (3.1)$$

where  $n_o$  and  $n_e$  are refractive indices of ordinary and extraordinary wave, respectively,  $d$  is the thickness of each wave plate, and  $c$  is the speed of light in vacuum,  $m$  is the order of the half-wave plates. On the other hand, the transmittance can be transferred into

$$T(\nu) = \left[ \frac{\sin\left(\frac{1}{2}\pi\sqrt{1 + \left(\frac{N\Delta\Gamma(\nu)}{\pi}\right)^2}\right)}{\sqrt{1 + \left(\frac{N\Delta\Gamma(\nu)}{\pi}\right)^2}} \right]^2, \quad (3.2)$$

where  $\Delta\Gamma(\nu)$  deviation of phase retardation,  $N$  is the number of wave plates, the FWHM at the central frequency is also given approximately by



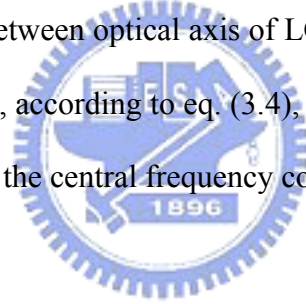
$$\Delta \nu_{\frac{1}{2}} \approx 1.60 \left[ \frac{\nu_m}{(2m+1)N} \right] \quad m=0, 1, 2, 3, \dots \quad (3.3)$$

where  $\nu_m$  is the central frequency respecting to the order of half wave plates

The large birefringence of LCs is well known and has been employed successfully for phase shifting of microwave and millimeter wave signals previously. In THz frequency range, we have recently determined the complex refractive index of a NLC E7 at room temperature by THz time-domain spectroscopy (THz-TDS) [9]. The birefringence of NLC:

$$\Delta n(\theta) = n_{eff} - n_o = \left[ \frac{\cos^2(\theta)}{n_o^2} + \frac{\sin^2(\theta)}{n_e^2} \right]^{\frac{1}{2}} - n_o \quad (3.4)$$

where  $\theta$  is the angle between optical axis of LC and direction of propagation of light, therefore, if we vary  $\theta$ , according to eq. (3.4), birefringence will be changed and then according to eq. (3.1), the central frequency could be tuned.



### 3.3. Design and measurement

Technologically, we apply two orientations of magnetic field to the same LC cells to avoid magnets blocking THz wave. Therefore, the large tunable range of two folded THz filter is obtained. One of two setups consists of two LC cells and two annular permanent magnets, which are fixed on rotary stages to re-orientate the molecules of LC as shown in the inset (a) of Fig. 3.3. The homeotropic LC cells are used in our filter. The cells are coated with N,N-dimethyl-n-octadecyl-3-aminopropyltrimethoxysilyl chloride (DMOAP) [10], to align the LC molecules perpendicular to the surface of fused silica plates. Each cell is constructed with two fused silica plates with aluminum spacers and filled with E7 (Merck) whose  $n_e$  and  $n_o$

are about 1.71 and 1.57 in the THz frequency range. The LC-based Solc filter has two folded retarders which are placed between a pair of parallel wire-grid polarizers (Specac, No. GS57204 with an extinction of  $> 1000$ ). The LC cells as tunable retarders (TR) are at the center of the rotatable magnet. TRs are oriented at  $22.5^\circ$  and  $-22.5^\circ$  with respect to the polarization of input light used to achieve the desired variable phase retardation,  $\Delta\Gamma$  (Fig. 3.3).

The thickness of LC layers is 5.7 mm. The threshold field required to reorient LC molecules in the LC cell when the magnetic field is perpendicular to the alignment direction is less than 0.001 Tesla [11]. The maximum magnetic field at cell position in the rotary permanent magnets (sintered Nd-Fe-B) is 0.427 Tesla ensuring that all LC molecules are parallel to the magnetic field. The retardation provided by homeotropic cells-TRs is zero when the direction of LC molecules is parallel to the z-axis and changes with the reorientation of the LC molecules by rotating magnets.

The other setup consists of the same LC cells but two pairs of cylindrical magnets, which are also fixed on rotary stages to re-orientate the molecules of LC as shown in the inset (b) of Fig. 3.3. The LC cell is put in the middle of two magnets and LC cells are reoriented at the same mechanism to achieve a desired variable phase retardation,  $\Delta\Gamma$ . Fig. 3.4 also shows experimental pictures of the LC-based tunable THz Solc filter, relative to the schematic diagram in Fig. 3.3 (a) and (b), respectively.

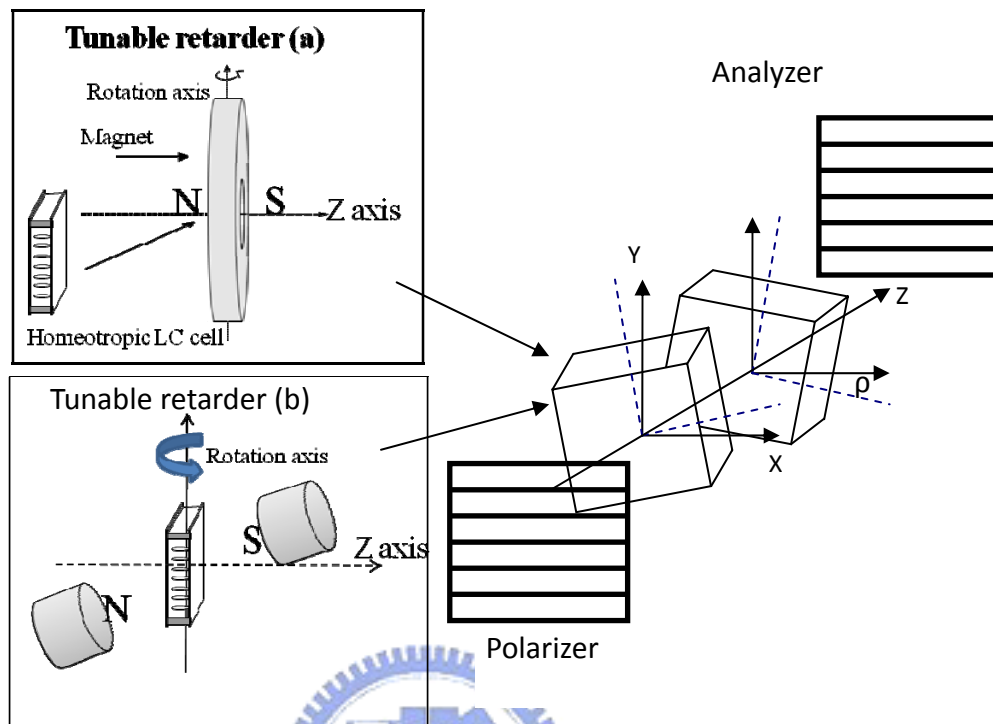


**Fig. 3.3. Schematic diagram of the LC-based tunable THz Solc filter. The inset (a) and (b) show two different ways to apply magnetic field on the same tunable LC THz retarders, respectively.**

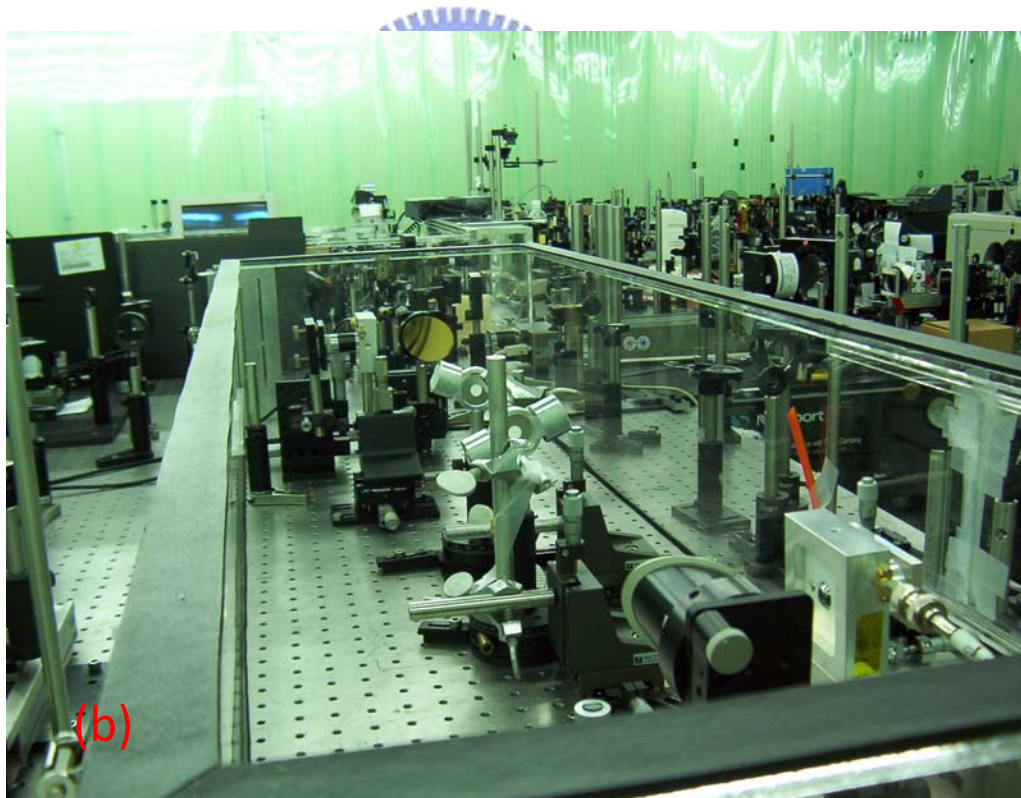
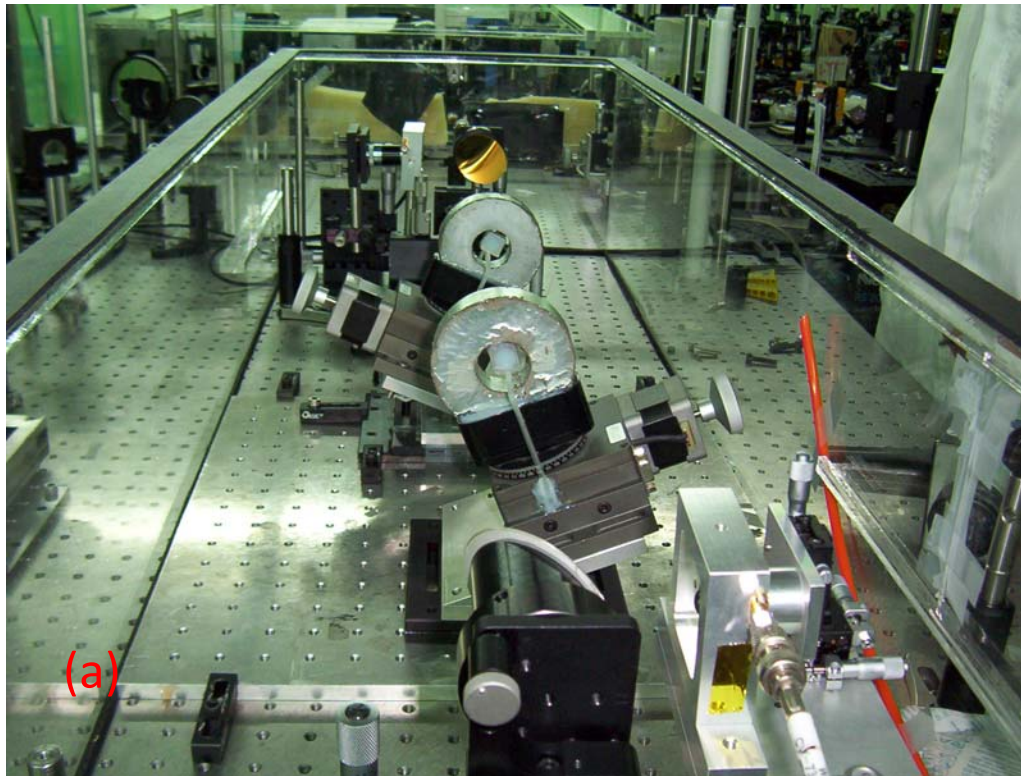


**Fig. 3.4. Experimental setup of the LC-based tunable THz Solc filter. The Fig. (a) and (b) refer to the schematic diagram in Fig. 3.3 (a) and (b), respectively.**

However, the magnetic field at LC cell position in this setup is 0.19 Tesla which is large enough to align all LC molecules. The retardation provided by TRs is the maximum when the direction of LC molecules is perpendicular to the z-axis and decreases with changing the rotating angle of magnets. Besides filling E7 in the homeotropic cell, we filled LC-DN125262W (daily polymer corporation) in homogeneous cells, which are coated with polyimide following by rubbing to align the LC molecules parallel to the surface of fused silica plates, and with aluminum spacers. Therefore, the high birefringence ( $\sim 0.18$ ) LC-DN125262W made the central pass-band frequency lower. The characteristics of DN125262 such as refractive indexes have been discussed in Sec.2.5.

The filter was characterized by using a photoconductive-antenna-based THz time-domain spectrometer (THz-TDS) [12]. In short, the pump beam from a femtosecond mode-locked Ti:sapphire laser illuminated the antenna fabricated on low-temperature-grown GaAs to radiate the broad band THz pulse, which was collimated and propagated through the filter. The transmitted THz pulse was monitored by the probe beam from the same laser and the same kind of antenna. The measurements are done at room temperature ( $\sim 25^\circ\text{C}$ ).

### 3.4. Results

Fig. 3.5 shows the spectral transmittance of the filter filled with E7, converted by taking into account the parallel-polarization configuration, at the  $90^\circ$  between magnetic field and z axis. The transmitted peak frequencies are 0.176 THz, 0.556 THz, 0.892THz, periodically, which is consistent with the relation in formula (3.1). The theoretical curves (solid curves) are also shown and calculated by considering the absorption of LC molecules [9], which is in good agreement with the experimental data.

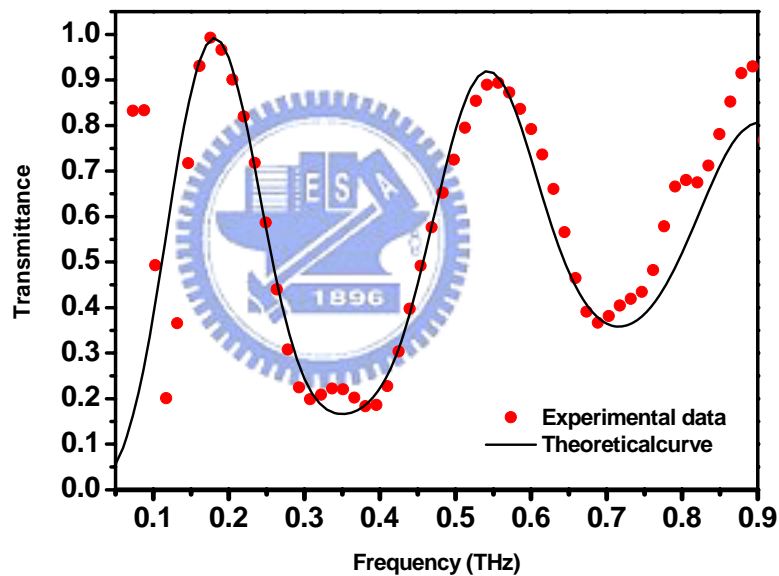


**Fig. 3.5.** An example of the transmittance of the broadband THz pulse through LC Solc filter filled with E7. The circles are experimental data and the solid line is theoretical prediction.

Furthermore, with the rotation angle from  $90^\circ$  to other smaller angles, transmitted THz spectrum of the filter is shifted to higher frequencies; the band width at higher frequencies is larger than the lower one. For example in Fig. 3.6, with the



rotation angle from  $90^\circ$  to  $70^\circ$ , transmitted THz spectrum and the band width are both in accord with the formula (3.2) and (3.3) respectively. On the other hand, although the imaginary parts of ordinary and extraordinary refractive indexes ( $\kappa_o$ ,  $\kappa_e$ ) of NLC are different, result in filtering effect imperfect, central pass-band frequencies are almost the same as prediction. This phenomenon can be explained by the coupled mode theory [1]. Two energy modes are coupled in this quasi-period filter. The incident light is converted from one mode to the other, as the phase matching condition is satisfied. While considering the difference between  $\kappa_o$  and  $\kappa_e$ , the phase matching condition will be not satisfied and energy can't be transformed completely. Therefore, it confines the filtering effect of a THz Solc filter.

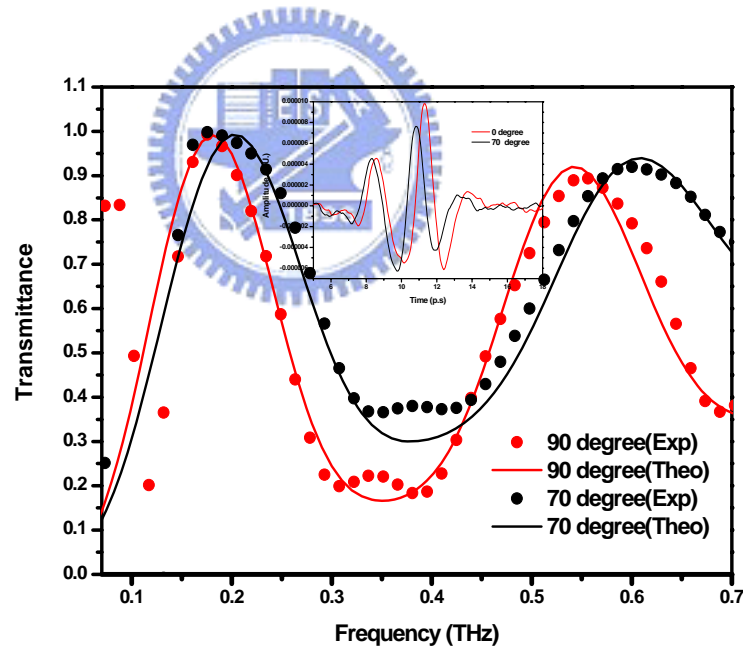


**Fig. 3.6.** An example of the transmitted spectrum of the broadband THz pulse which is tuned using a LC (E7) THz Solc filter. The insert is time domain profiles. The circles and squares are experimental data and the solid lines are the theoretical prediction.

According to the dexterous tunable retarders in Fig. 3.3, the first order central frequency of a Solc filter is tuning from 0.176 to 0.793 THz (Fig. 3.7) by rotating the magnetic field from  $90^\circ$  to  $30^\circ$  referring to z axis. Therefore, tunable range of a THz filter is largely improved.

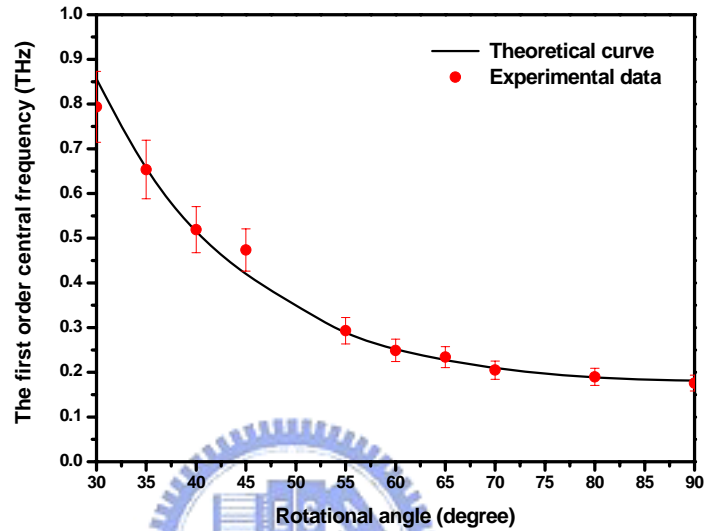


**Fig. 3.7. The first-order central frequencies of the filter filled with E7 versus rotation angle  $\theta$  between magnetic field and z axis. The circles are experimental data. The curve is theoretical calculation.**

Besides infusing E7 into the 5.7mm LC cells, we also infused DN125262W-high birefringence LC into 3.15mm LC cells to reduce thickness of the filter. Although this kind of LC has larger birefringence, its absorption increases with frequency apparently, so that it is hard to use in higher frequencies. The insertion loss is  $\sim 3.7$  dB at 0.3THz. If we compare with results of E7, it reduces the insertion to  $\sim 1.5$ dB. Fig. 3.8 is another example of LC solc filter filled DN125262W; Fig. 3.9 is the relation between rotation angle and the first order central frequency. Therefore, no matter which kind of LCs is applied, the experimental results both consistent with the theoretical calculation.



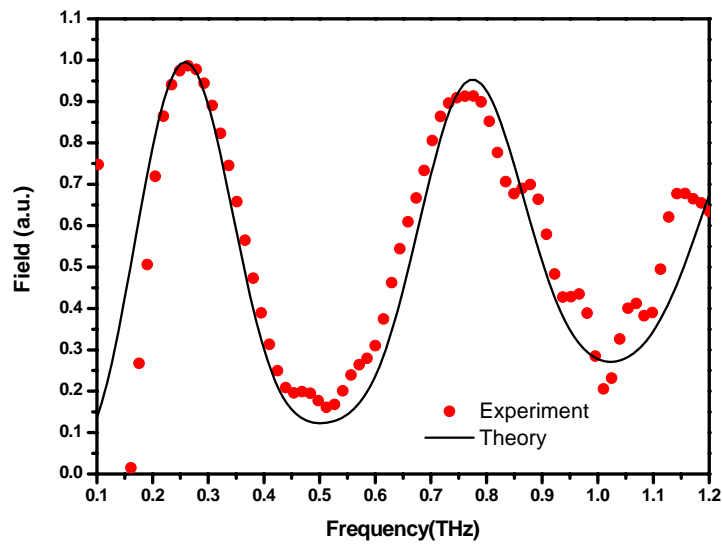


**Fig. 3.8.** An example of the transmitted spectrum of the broadband THz pulse through LC Solc filter filled DN125262W. The circles are experimental data and the solid line is theoretical prediction.

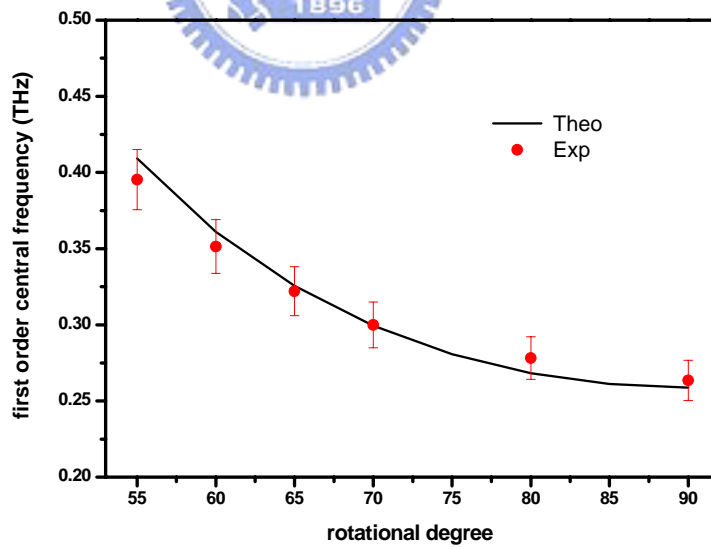


**Fig. 3.9.** The central transmitted frequencies of the filter filled with DN125262W versus rotation angle  $\theta$  between magnetic field and z axis. The circles are experimental data. The curve is theoretical.

### 3.5. Discussion

Fig. 3.10 (a) and (b) shows the profiles in time domain of the Solc filter and the reference cell whose THz polarization is parallel to the direction of LC molecules. Theoretically, a THz wave through the filter is separated into three main peaks, which can be understood as following: the THz wave is separated into o-ray and e-ray after passing the first LC cell and further these two waves are separated into o-o ray, o-e ray, e-o ray, and e-e ray after passing the second one. Moreover, two LC cells have same retardations so that e-o ray and o-e ray overlap with each other; again e-e ray with the largest retardation overlaps with the main signal of the reference (ne) due to the same total thickness between filter and reference cells; o-o ray with the smallest retardation is the early signal, but due to the larger absorption according to  $\kappa_o$  comparing with  $\kappa_e$  [9], the o-o ray is not revealed apparently. Therefore, in Fig. 3.6 only two main peaks are appeared in the time domain profile of this Solc filter. Besides, we also calculate the time delay between each peak. In E7 based filter, the time delay between e-e ray and o-e (or e-o) ray is 2.755 ps theoretically, which is closed to 2.735 ps in the measurement; in DN125262 based filter, the time delay between e-e ray and o-e (or e-o) ray is 1.932 ps theoretically, which is closed to 2.001 ps in the measurement.

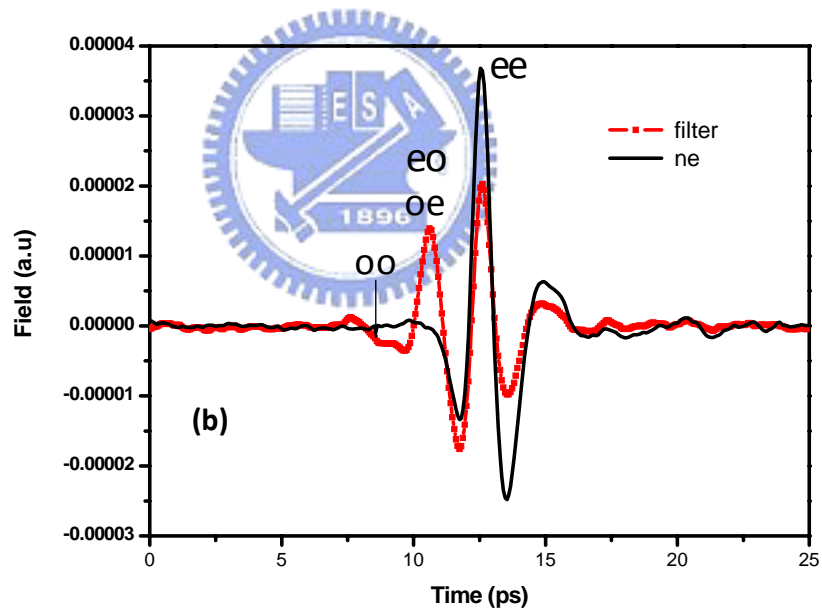
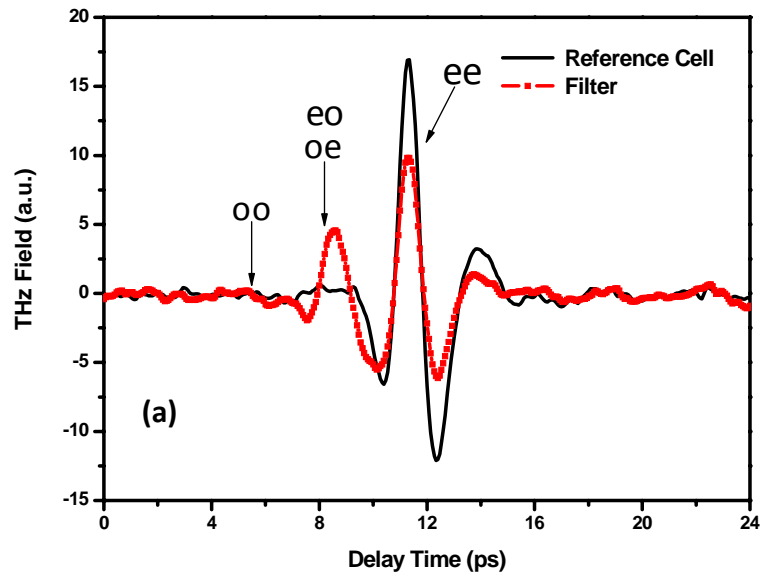


**Fig. 3.10.** The temporal profiles of a THz pulse through (a) E7 based Solc filter and reference LC cells (b) DN125262W based Solc filter and reference ones.

### 3.6. Comparison with our previous work: a THz Lyot filter

Comparing with our previous work, a THz tunable Lyot filter [13] whose tuning range is from 0.388 to 0.564 THz and insertion loss is 8 dB. However, the tunable range of THz E7 based Solc filter is largely increased from 0.176 to 0.793 THz and the insertion loss is about 5 dB. Moreover, two elements utilized in the Solc filter instead of four elements used in the Lyot filter, we promote practicability and convenience of a THz filter. Furthermore, a Lyot filter has intrinsic confinement of different thicknesses in each retarder whereas a Solc filter can have a uniform thickness easily operated in various designs.

	<b>Lyot</b>	<b>Solc</b>
<b>Setting</b>	4 components	2 components
<b>Tunable Range</b>	0.388~0.564THz (0.18THz)	0.176~0.794THz (0.61782THz)
<b>Bandwidth</b>	0.1THz	0.117~0.465THz
<b>Insertion Loss</b>	~8dB	~5dB
<b>Natural</b>	Non-filtering low frequency	Easily used in any frequency
<b>Confinement</b>	waves fixed at zero	range

**Table 3.1. The comparison of Lyot and Solc filter in THz range.**

### 3.7. Summary

We have demonstrated for the first time a large tunable range, room-temperature THz Solc filter. The key elements are variable LC phase retarders and the genius design, applying magnetic field to LC molecules, increases the tunable range of a THz filter. The first central pass-band frequency in E7 cells can be continuously tuned from 0.176 THz to 0.793 THz and the insertion loss is about 5 dB. We also fabricate another high birefringence LC cells (DN125262W) as retarders. The experimental data of these two types of Solc filters are both in good agreement with theoretical predictions. Still narrower bandwidth is feasible by cascading more elements.



### 3.8. References

1. A. Yariv and P. Yeh, *Optical Waves in Crystal: Jones Calculus and its Application to Birefringent Optical Systems*. (Wiley, New York, 1984)
2. B. Lyot, "Optical apparatus with wide field using interference of polarized light," *C.R. Acad. Sci. (Paris)* **197**, 1593 (1933).
3. B. Lyot, "Filter monochromatique polarisant et ses applications en physique solaire," *Ann. Astrophys.* **7**, 31 (1944).
4. Y. Ohman, "A new monochromator," *Nature* **41**, 157, 291 (1938).
5. Y. Ohman, "On some new birefringent filter for solar research," *Ark. Astron.* **2**, 165 (1958)
6. Czechoslovak Cosopis pro Fvsiku, "Solc elements in Lyot-Ohman filters," *J. Optics (Paris)* **11**, 293-304 (1980).
7. I. Solc, "Birefringent chain filters," *J. Opt. Soc. Am.* **55**, 621–625 (1965)
8. X. Chen, J. Shi, Y. Chen, Y. Zhu, Y. Xia, and Y. Chen, "Electro-optic Solc-type wavelength filter in periodically poled lithium niobate," *Opt. Lett.* **28**, 2115-2117 (2003).
9. C.-Y. Chen, C.-F. Hsieh, Y.-F. Lin, R.P. Pan, and C.-L. Pan, "Magnetically tunable room-temperature  $2\pi$  liquid crystal terahertz phase shifter," *Opt. Express* **12**, 2630-2635 (2004)
10. F. J. Kahn, "Orientation of liquid crystals by surface coupling agents," *Appl. Phys. Lett.* **22**, 386-388 (1973).
11. P. G. de Gennes and J. Prost, *The Physics of Liquid Crystals*, **2nd ed.** (Oxford, New York, 1983).
12. S. Nashima, O. Morikawa, K. Takata, and M. Hangyo, "Temperature dependence of optical and electronic properties of moderately doped silicon at terahertz

frequencies,” J. Appl. Phys. **90**, 837-842 (2001).

13. C.-Y. Chen, C.-L. Pan, C.-F. Hsieh, Y.-F. Lin, and R.P. Pan, “Liquid-crystal-based terahertz tunable Lyot filter,” Appl. Phys. Lett. **88**, 101107 (2006).



# Chapter4. Electrically Controlled Liquid-Crystal-Based Terahertz Tunable Solc Filter

## 4.1. Introduction

Recently, we have demonstrated the electrically controlled liquid-crystal THz phase shifter [1]. Here, we propose to study and design an electrically controlled THz Solc filter by using LC elements. We will use a pair of precision-machined copper electrodes to support electric field to rotate the direction of the LC molecules. The effective refractive index of LC will be changed with the rotation of the molecules. Therefore, the modulated phase retardation can be achieved. The experimental results will be compared with simulation calculation and explained by theory. Furthermore, we will design the THz tunable Solc filter with four LC elements. The device can be used on THz biological nondestructive testing; besides, this could be tuned by electric field in a great range.

## 4.2. Previous evaluation

Before starting this work, we make some simulations of electric field distribution between electrodes in an empty LC cell with Comsol Multiphysics 3.2. The Fig. 4.1 is the result under the following condition. Two fused silica plates are separated by a pair copper electrode spacers. The distance and cut edge between two electrodes is 1.5 cm and  $45^\circ$  referring to horizontal line; the area and thickness of



copper is 5 cm<sup>2</sup> and 1.5 mm, respectively; applying voltage on electrodes is 100 volt. Therefore, the electric field distribution between two electrodes is almost uniform, strong, and vertical to the edge of coppers whereas outside the spacer the electric field is not uniform and become relatively smaller. It was good news for us that as we infused LCs in the spacer, we just measured the central part of it.

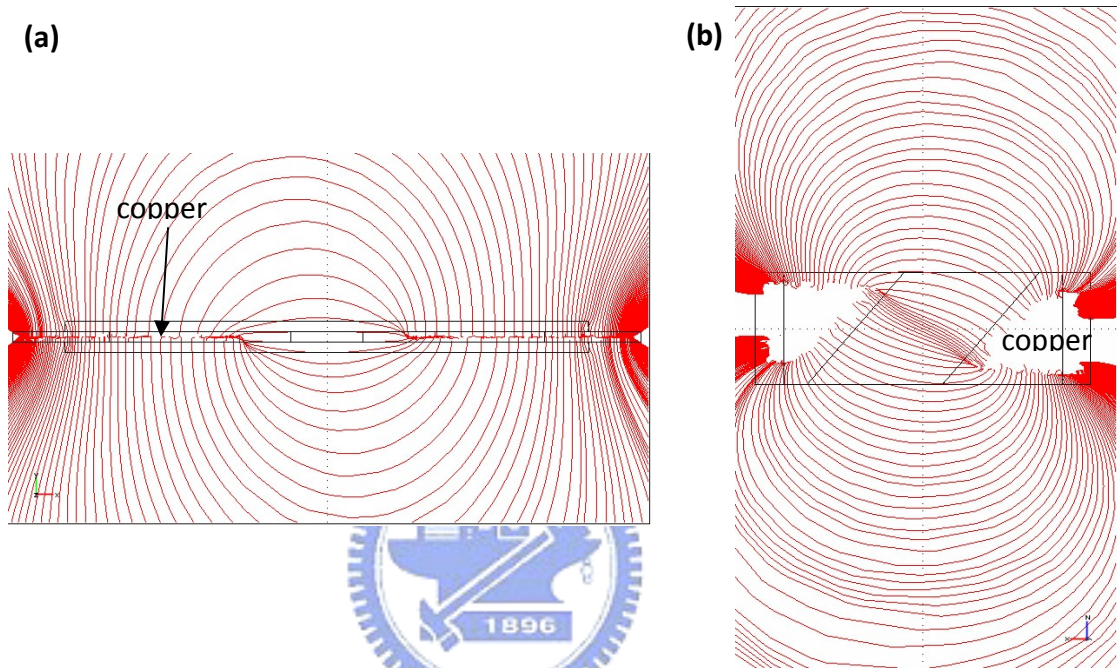


**Fig. 4.1. The simulation results of electric field distribution between electrodes in an empty LC cell (a) in a lateral view (b) in a top view. (Simulated by T.T. Tang )**

### 4.3 Sample preparation and setup

The construction of the sample is shown in Fig 4.2. Each fused silica plate with an area of 4.5 cm by 2.5 cm is employed. The cell is filled with LC, E7 (Merck). We use copper spacers for controlling the thickness of LC layers to 1.5 mm each. The coppers that provide electric field for tuning the phase retardation of the THz wave, was employed. The distance between two coppers is 18mm. The inner surfaces of the plates are coated with DMOAP such that the LC molecules are initially

perpendicular to the substrates [2]. One element of a tunable LC THz Solc filter is shown in Fig. 4.3. The propagation direction of THz wave is along Z axis and the direction of applied electrical field is tilted with  $22.5^\circ$  or  $-22.5^\circ$  referring to X axis.

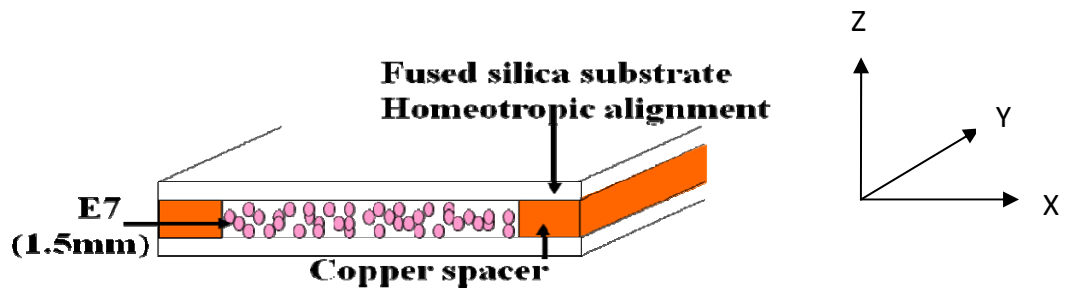


**Fig. 4.2.** The schematic diagram of homeotropic alignment LC cell. The cell gap is 1.5mm.

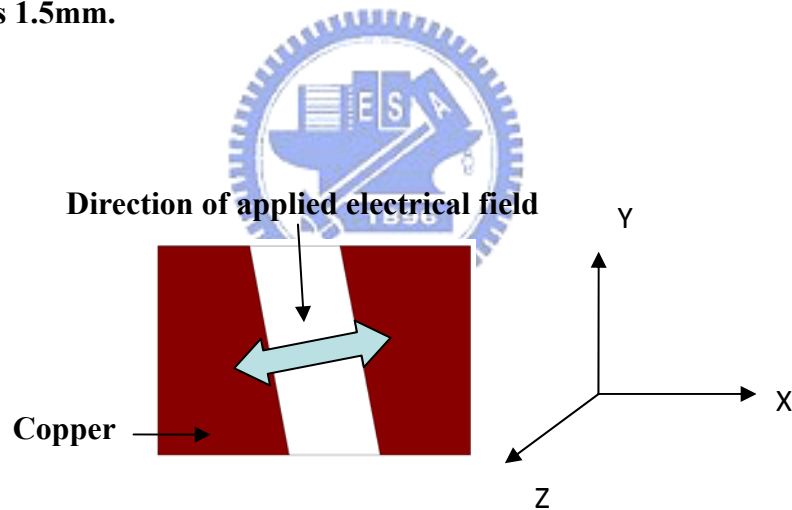


**Fig. 4.3.** The schematic diagram of one element in a tunable LC THz Solc filter. The propagation direction of the THz wave is along Z axis. The direction of applied electrical field is tilted with  $22.5^\circ$  or  $-22.5^\circ$  referring to X axis.

The arrangement of a tunable two folded THz Solc filter based on electric controlled retardation in LC is shown in Fig. 4.4. The applied electrical field directions have tilting angles  $22.5^\circ$  and  $-22.5^\circ$  with respect to the polarization of input light respectively.

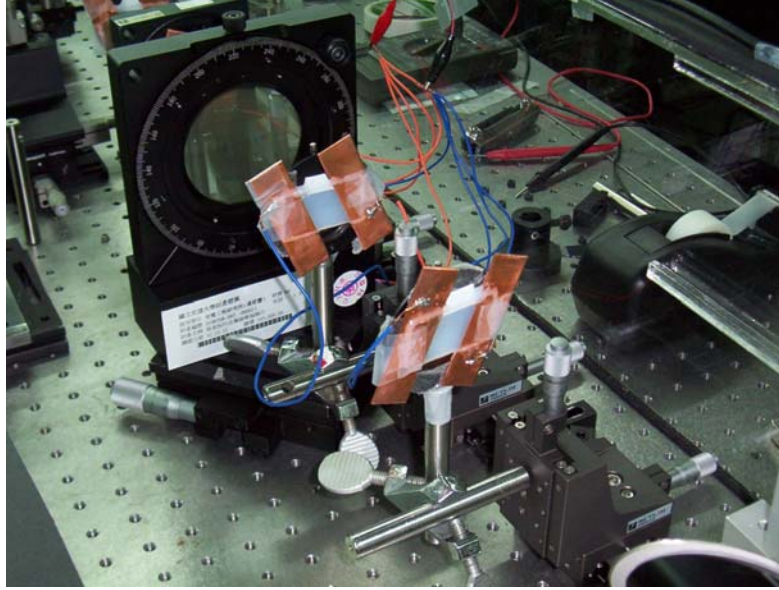


**Fig. 4.4. The experimental picture of the two folded THz Solc filter based on LCs.**

The tunable retarder elements are our electrical controlled THz phase shifter, i.e., a homeotropically aligned LC cell are controlled by a pair of coppers as electrodes to achieve the desired variable phase retardation,  $\delta(v)$

$$\delta(\theta) = 2\pi L \frac{f}{c} \left\{ \left[ \frac{\cos^2(\theta)}{n_e^2} + \frac{\sin^2(\theta)}{n_o^2} \right]^{\frac{1}{2}} - n_o \right\}, \quad (4.1)$$

where L is the thickness of LC layer, f is the frequency of the THz waves, c is the speed of light in vacuum,  $n_o$  and  $n_e$  are the ordinary and extra-ordinary refractive indices of the LC.  $\theta$  is the angle between the polarization direction of electricomagnetic wave and the pricipal axis of LCs. The theoretical phase retardation can be calculated as we know the  $n_o$  and  $n_e$  of LC.

With positive dielectric anisotropy, the E7 molecules in the bulk of the cell will be reoriented toward the applied electric field if the field is increased beyond the

threshold voltage (the Freedericksz transition),  $V_{th} = \pi \left( \frac{L}{d} \right) \times \left( \frac{k_3}{\epsilon_a \epsilon_0} \right)^{\frac{1}{2}}$  [3], where L is the distance between two electrodes, d is thickness of the NLC layer, and  $k_3$ ,  $\epsilon_a = \epsilon_{//} - \epsilon_{\perp}$ , and  $\epsilon_0$  are the bend elastic constant, dielectric anisotropy, and electric permittivity of free space, respectively. We change the applied voltage from 0 to 50V and the threshold voltage ( $V_{th}$ ) in our work is  $\sim 13.4V$ , with  $L=18mm$ ,  $d=1.5mm$ ,  $k_3 = 17.1 \times 10^{-12} N$ , and  $\epsilon_a = 13.8$  (from Merck). The applied voltages quoted in this paper are all rms values. The retardation provided by homeotropic TRs are zero when the LC molecules are parallel to the z-axis and change by varying the applied voltages. Fig. 4.5 is a schematic diagram of LC molecules orientating under different fields. The filter was characterized by using a photoconductive-antenna-based terahertz time domain spectroscopy (THz-TDS) [4]. The measurements are done at room temperature ( $\sim 25^\circ C$ ).

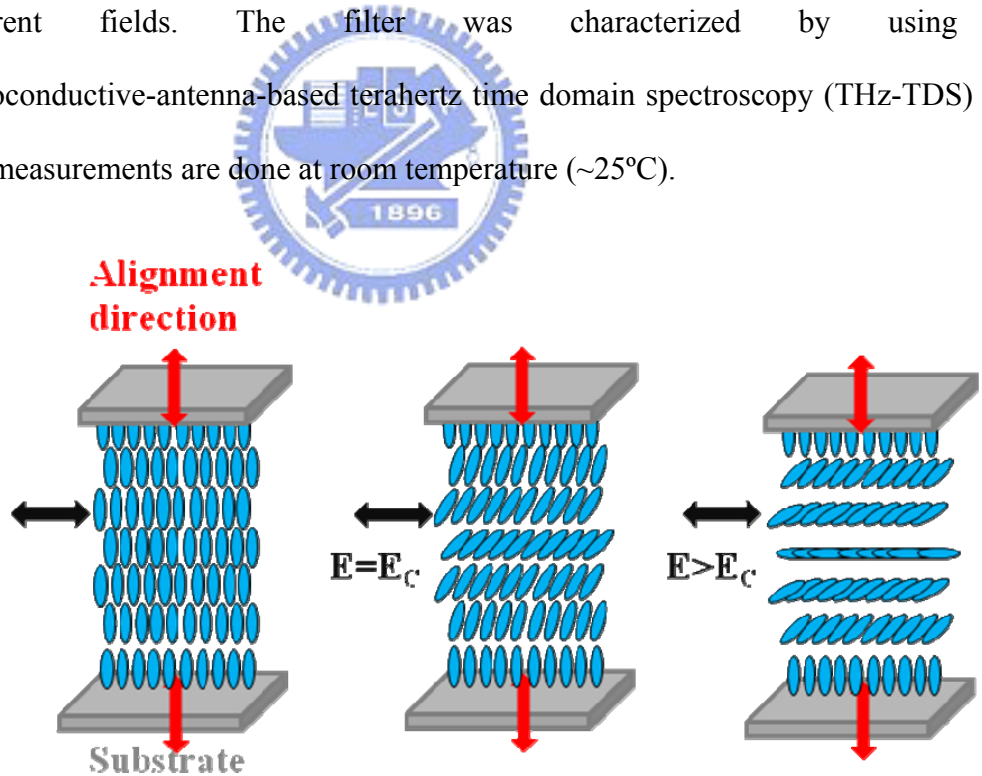


**Fig. 4.5. A schematic diagram of LC molecules orientating under different fields.  $E_c$  is the threshold voltage and  $E$  is the applied field.**

## 4.4 Results and discussion

Fig. 4.6 shows the power transmittance of this device, converted by taking into account the parallel-polarization configuration, with applied voltage tuned from 15 to 25V, normalized to the maximum of transmittance. The theoretical curves are shown as the solid curves. As applied voltage is increased to 22.5V, the central frequency of the Solc filter is tuned to 0.908 THz. At 25V, the central frequency shifts to 0.761 THz. This is consistent to the theoretical prediction. However, the profile of experimental result is narrower than theoretical prediction, which can be explained by the phenomenon observed in experiment. When we apply voltage on the LC molecules, the molecules flowed around the edge inside LC cells. Moreover, the larger applied voltage, the stronger flowing effect. According to the convective instabilities under electric fields [3], the alignment in a nematic single crystal may be destroyed by a rather small voltage (of the order of 10V) applied between two points in the sample. If the voltage is increased above the voltage threshold  $V$ , the distortion amplitudes and the associate flow velocities increase. Therefore, the LC molecules can't orient the direction uniformly, especially as the applied voltage larger, which largely affect filter ability in this work.

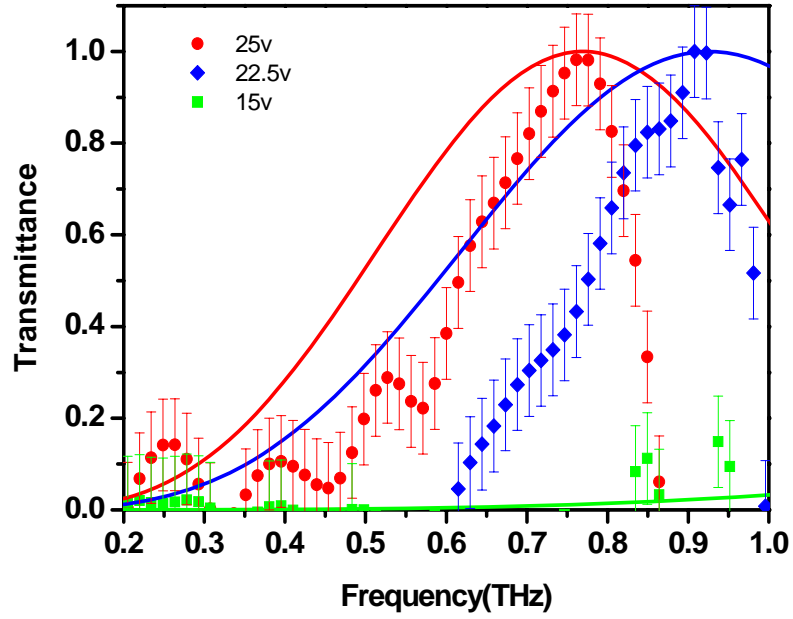


**Fig. 4.6 Spectra of the transmitted broadband THz pulse through the LC THz Solc filter at several voltages. The circles, diamonds and squares are experimental data and the solid lines are the theoretical prediction.**

For  $V > V_{th}$  the angle  $\theta$  at any point  $z$  in the cell can be computed by using the relation [5].

$$\frac{z}{d} = \frac{V_{th}}{\pi V} \int_0^{\theta} \left( \frac{1 + q \sin^2 \theta}{\sin^2 \theta_m - \sin^2 \theta} \right)^{\frac{1}{2}} d\theta, \quad (4.2)$$

where  $q = (k_1 - k_3)/k_3$ ,  $k_1$  ( $= 11.1 \times 10^{-12} N$  for E7) and  $k_3$  ( $= 17.1 \times 10^{-12} N$  for E7) are the splay and bend elastic constant of NLC. The angle  $\theta_m$  is the maximum reorientation angle located at  $z=d/2$ .

$$\frac{V}{V_{th}} = \frac{2}{\pi} \int_0^{\theta_m} \left( \frac{1 + q \sin^2 \theta}{\sin^2 \theta_m - \sin^2 \theta} \right)^{\frac{1}{2}} d\theta, \quad (4.3)$$

Equations (4.1)-(4.3) allow us to calculate the birefringence of LC molecules in the



cell for a given applied voltage. Fig. 4.7 shows the central pass band frequency is tuned from 0.717 to 1.142 THz by changing voltage. The solid curve is theoretical prediction according to Eqs. (4.1)-(4.3) and the circles are experimental data.

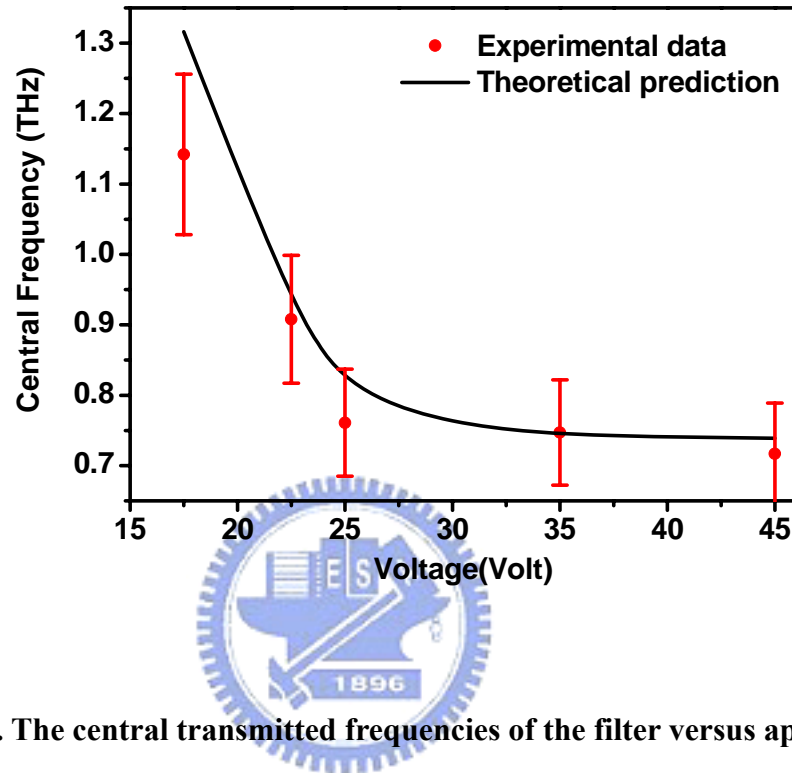


**Fig. 4.7. The central transmitted frequencies of the filter versus applied voltages. The circles are experimental data. The curve is theoretical line**

Moreover, according to Eq. (3.1), doubling the thickness of the wave plates, the central frequency become half. Fig 4.8 shows that when the thickness of wave plates is increased from 1.5 mm to 3.0 mm, the central frequency changes from 0.761THz to 0.395 THz.

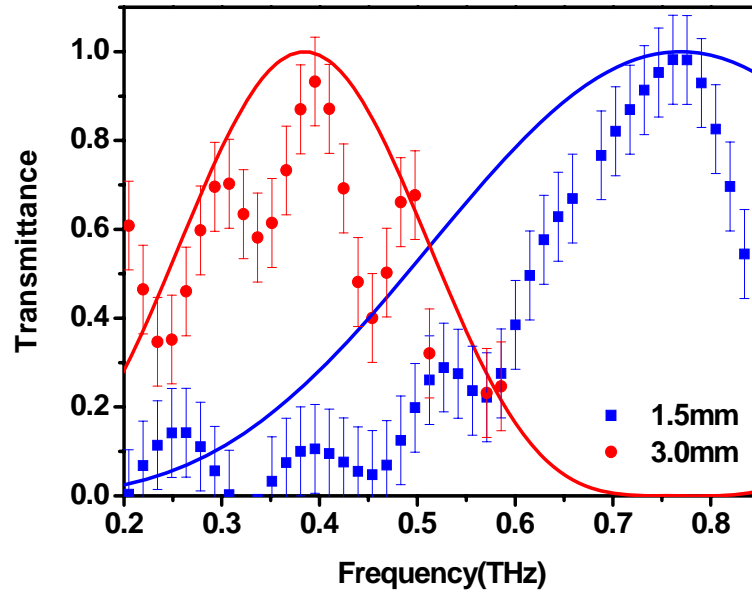
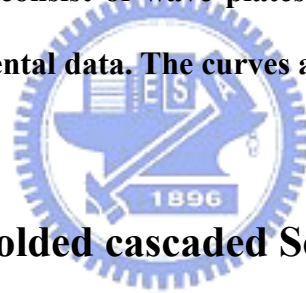


**Fig. 4.8.** Solc filters consist of wave plates of two thicknesses. The circles and squares are experimental data. The curves are theoretical prediction.



#### **4.5. A four-stage folded cascaded Solc filter**

In this section, we will discuss more elements which were cascaded together in the filter to reduce space of alignment and increase the practicability. On the other hand, large birefringence LCs has been investigated in section 2.5, so that we also filled DN125262W in these cells to make central frequency lower. Besides, each element A, B, C, and D have the same construction as shown in Fig 4.2; the applied electrical field directions have tilting angles  $11.25^\circ$  and  $-11.25^\circ$  alternatively with respect to the polarization of input light respectively as shown in Fig. 4.9.



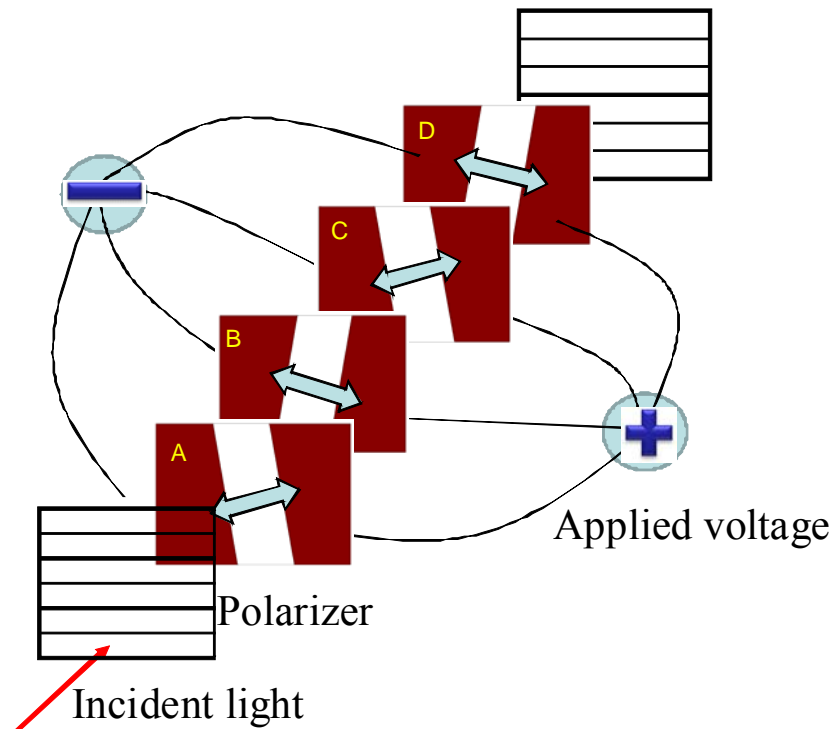


**Fig. 4.9. The schematic diagram of a tunable four folded cascaded THz Solc filter.**



Fig. 4.10 is the result of the four-stage folded filter, converted by taking into account the parallel-polarization configuration. Apparently the central frequency is tuned from 0.6THz to 0.48THz with applied voltage from 19.6 rms to 26.2 rms. However, we only get the qualitative analysis, and the more quantification is still to be done after more parameters of DN125262W is investigated in THz range and more clear dynamics behavior is understood.

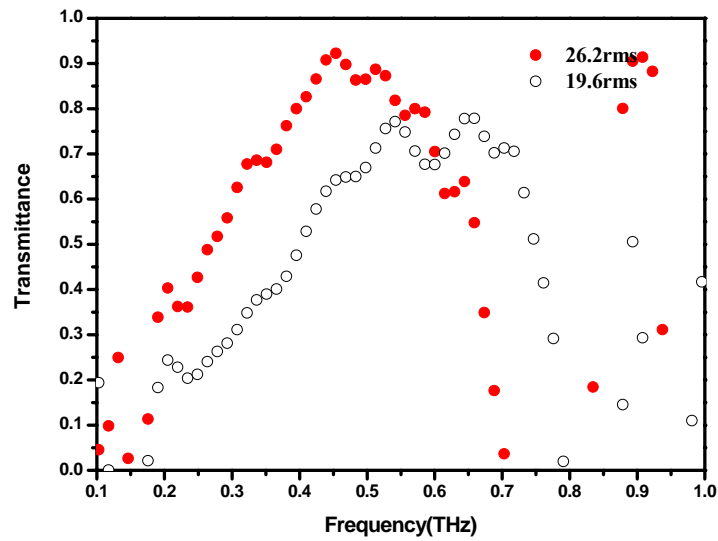


**Fig. 4.10. Spectra of the transmitted broadband THz pulse through the four folded Solc filter at two voltages.**

## 4.6 Improvement

The electrically controlled THz Solc filter has many advantages of compact use, ease in control, fast response, and low insertion loss. However, convective instabilities of LC molecules under electric fields affect the filtering ability. Besides, the tunable retarder is achieved by two forces: surface anchoring force and applied electric force to which the LC molecules are subjected. After applied voltage increases to the threshold voltage, the LC molecules are sensitive to orient their director. Therefore, it is a sharp increase of birefringence with applied voltage; the central frequency is tuned from high frequency to low frequency in a short voltage range. It is hard to decide the voltage range exactly since the LC molecules flow in the cells, and plating surfactant and the thickness of cells also influence on LC molecules. Therefore, how to reduce the flow instability under electric field and control the strength of surface anchoring force is still worth investigating.

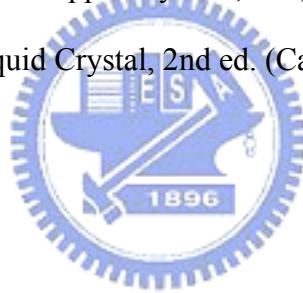
## 4.7 Summary

We have demonstrated for the first time, an electrically controlled, tunable THz Solc filter. The key elements are variable LC phase retarders. The central pass-band frequency of the filter with E7 can be continuously tuned from 0.717 to 1.142 THz. We also fabricate a four-stage folded cascaded Solc filter with high birefringence LCs (DN125262W), which also have filtering effect. Moreover, doubling the thickness of the filter, the central frequency is changed from 0.761 to 0.395 THz in a good agreement with theoretical predictions.




## 4.8 References

1. C.F. Hsieh, and R. P. Pan, T.T. Tang, H.L. Chen, and C.L. Pan, “ Voltage-controlled liquid-crystal terahertz phase shifter and quarter-wave plate,” *Opt. Lett.* **31**, 1112-1114 (2006).
2. F. J. Kahn, “Orientation of liquid crystals by surface coupling agents,” *Appl. Phys. Lett.* **22**, 386-388 (1973).
3. P. G. de Gennes and J. Prost, *The Physics of Liquid Crystals*, 2nd ed. (Oxford,1983).
4. S. Nashima, O. Morikawa, K. Takata, and M. Hangyo, *J. Appl. Phys.* “Temperature dependence of optical and electronic properties of moderately doped silicon at terahertz frequencies,” *J. Appl. Phys.* **90**, 837, 2001.
5. S. Chandrasekhar, *Liquid Crystal*, 2nd ed. (Cambridge, 1992)



## Chapter5. Conclusion and Future Work

We have demonstrated for the first time a large tunable range, room-temperature THz Solc filter. The key elements are variable LC phase retarders and the genius design, applying magnetic field to LC molecules, increases the tunable range of a THz filter. The first central pass-band frequency in E7 cells can be continuously tuned from 0.176 THz to 0.793 THz (a fractional tuning range of 350 %) and the insertion loss is about 5 dB. We also fabricate another high birefringence LC cells (DN125262W) as retarders. The experimental data of these two types of Solc filters are both in good agreement with theoretical predictions. Still narrower bandwidth is feasible by cascading more elements.



Besides, although convective instabilities of LC molecules under electric fields, the electrically controlled THz Solc filter still has many advantages of compact use, ease in control, fast response, and low insertion loss. We demonstrated an electrically controlled, tunable THz Solc filter with E7 of which central pass-band frequency can be continuously tuned from 0.717 to 1.142 THz. We also fabricate a four-stage folded cascaded Solc filter with high birefringence LCs (DN125262W), which also have filtering effect. Moreover, doubling the thickness of the filter, the central frequency is changed from 0.761 to 0.395 THz in a good agreement with theoretical predictions. However, how to reduce the flow instability under electric field and control the strength of surface anchoring force is still worth investigating.

Furthermore, some groups have applied electrical field on periodically poled lithium niobate (PPLN), a Solc-type filter can be realized in near infrared range. Again, in the past decade, PPLN has widely studied in the field of nonlinear optical interactions

in THz range. In the future work, the development and design of a new nonlinear crystal-based filter in THz range will be promising.

